ELSEVIER

Contents lists available at ScienceDirect

International Journal of Mechanical Sciences

journal homepage: www.elsevier.com/locate/ijmecsci





Novel method to assess anisotropy in formability using DIC

Ebrahim Seidi a,*, Scott F. Miller b, Farnaz Kaviari b, Lu Huang c, Thomas B. Stoughton c

- ^a Lamar University, Beaumont, TX, USA
- ^b University of Hawaii at Manoa, Honolulu, HI, USA
- ^c Global Technical Center, General Motors, Warren, MI, USA

ARTICLE INFO

Keywords:
Material anisotropy
Mathematical analysis
Material deformation
Forming limit
Curvature method
Digital image correlation
Localized neck

ABSTRACT

In this study, a novel technique was developed to identify localized neck of a tensile sample based on the curvature of the surface that is expected to work with any metal in which a localized neck forms prior to fracture. Moreover, a MATLAB-based computational tool has been developed to conduct advanced mathematical computations and numerical analysis on data generated from uniaxial tensile test of DP980 steel coupled with Digital Image Correlation (DIC) based on the novel curvature method. The presented curvature technique is a geometry-based approach that uses the specimen's surface profile and groove geometry to detect localized necking, avoiding the limitations of strain-based methods in distinguishing between localized and diffuse necking. A detailed analysis was conducted on the accuracy of the onset and anisotropy of localized neck. The results of the study revealed that specimens fabricated with 30-degree orientation with respect to the Rolling Direction (RD) of the sheet metal, exhibit a higher level of total strain at the onset of the localized necking, indicating the influence of anisotropy on the material's behavior for DP980. Moreover, consistent R-values were observed among specimens with the same orientation with respect to the RD, exhibiting a rising trend of R-value for orientations from zero to 60-degree, followed by a decrease from 60 to 90-degree. Furthermore, the results exhibited a negative linear relationship between R-values and the magnitude of thinning strain.

1. Introduction

This paper presents a detailed analysis of data generated by Digital Image Correlation (DIC). DIC is a non-destructive and non-contact optical measurement technique that enables the real-time measurement of full-field displacements and strains in materials with a high spatial resolution through comparing digital images. The focus of the analysis was the identification of the onset of localized neck in tensile samples. The local or through-thickness neck is characterized by a narrow band of deformation that forms shortly before fracture. One of the challenges in the automotive industry is accurate determination of the necking and fracture limits in metals as a measure of formability in the stamping of sheet metal components and in their product performance [1]. In addition to serving as a deformation limit in sheet metal stamping operations, the accurate identification of onset of localized necking plays a determining role in initiation of fracture, characterizing materials, assessing structural integrity, and optimizing design.

Following the occurrence of widespread diffuse necking after maximum load, the material proceeds through subsequent deformation phases in which strain concentration and localized necking arise within

the diffuse necking zone, prior to ultimate fracture [2]. The onset of localized necking signifies the stage at which the material initiates the manifestation of a groove in the sheet with a width determined by the sheet thickness, resulting in strain concentration far more severe than that caused by a diffuse neck. The emergence of the localized necking is associated with a prominent decrement in the cross-sectional area due to the excessive thinning and eventual material fracture. Upon the initiation of localized necking, the continued tensile force intensifies the localized necking. The sequence of events, starting with diffuse necking, followed by the emergence of localized necking, and ultimately leading to fracture, demonstrates the sequence of material failure mechanisms observed during a tensile test.

More broadly, DIC technique has been used extensively in the study of metal forming. Fang et al. [3] used DIC experimental data to calculate a more accurate R-value measurement. Nguyen et al. [4] used DIC to measure many properties of AL 5052-O and DP 980 steel including Poisson's ratio, anisotropic plastic ratio parameters, and flow curve in a uniaxial tension test. Wang et al. [5] created a complete strain profile of DP 600 from DIC data throughout the elastic and plastic regions of deformation. A comparison of four different time-dependent and

E-mail address: eseidi@lamar.edu (E. Seidi).

^{*} Corresponding author.

time/geometry-dependent necking criteria in their ability to detect the onset of necking of TRIP 780 sheet samples stretched formed over a hemispherical punch [6]. It was found that the geometry-dependent surface slope criterion was the most consistent, while the 3D-curvature criterion had the greatest sensitivity in detection of the onset of neck. It was shown that AA 6000 sheet metal follows the volume conservation assumption outside the necking band, but a significant increase in the volume strain was observed in all samples prior to failure in notched sheet metal coupons [7]. DIC has also been used to measure stress concentrations in samples with circular, square, and triangular notches [8]. A time-dependent and a time-position-dependent method were investigated for detection of onset of necking and evaluation of limit strains under significant through thickness strain gradients [9]. Li et al. [10] presented the true stress-strain curve of DP 780 from DIC measurement alongside theoretical curves.

DIC has also been studied more broadly in plastic deformation. Deformation in necking was studied for highly ductile and anisotropic materials [11]. They were able to reconstruct the necking geometry validated with DIC measurements. In another study of miniature samples, the fracture geometry and strain were examined [12]. A discontinuity tolerant DIC method was used for identification of slip system type and direction [13]. Large deformation was measured in a uniaxial tension test by DIC with half of the sample painted as in conventional DIC, and the other half is left unpainted and illuminated by a laser, called laser speckles, for remediation of paint delamination at large strain [14]. A simple study of the evolution of the necking region was done through DIC measurement of displacement of different points on the sample [15]. In more recent studies, four stereo, synchronized DIC systems were used to obtain detailed information about the displacement and strain field output [16]. 3D DIC analysis, where a left camera and right camera capture images on the thickness and width faces of the sample, resulted in wide strain range equivalent stress-strain curves [17]. The accuracy and uncertainty of DIC measurements have also been investigated [18, 19]. As shown, DIC has been developed and used to advance understanding of mechanical deformation and properties. The focus of this research is on the advanced plastic stage of localized necking, in which there is more limited study.

The contribution of this paper is the continuation of the curvature method for onset of localized neck detection, which has been previously introduced [20-22]. The methods for localized neck detection relevant to forming limits can be categorized as spatial methods [23,24], temporal methods [25–28], and spatial-temporal methods [9,29,30]. Localized neck has been determined from the area of the sample at different positions from DIC data [31], pronounced increase in average thickness strain [32], and spatial strain distribution [33]. It is thought that the curvature method has the advantage in detecting the onset of localized neck over other methods. In this method the geometrical curvature of the surface profile is determined at each step in the tension test. As the sample deforms throughout the tension test, initially, the surface profile and curvature changes are small. However, as the deformation reaches necking, the changes in profile are pronounced and noticeable, and even more so in the curvature. In light of the existing literature, the purpose of this research is to advance the accuracy of the curvature method for localized neck detection and characterize anisotropy of this phenomenon.

There have been extensive studies of the anisotropy of the constitutive behavior of sheet metal materials, with a few of the more recent studies reviewed here. El-Aty et al. [34] reviewed the literature on strengthening mechanisms, deformation, and anisotropic properties of Al-Li alloys. The literature shows properties are very anisotropic due to crystallographic texture and effects from the different phases. Stress-strain curves were shown with higher strength at 0° and 0° and lower strength at 0° degrees from rolling direction. Aleksandrovic et al. [35] studied the variation of the R-value for DC04 steel, AlMg4.5Mn0.7 and stainless steel X5CrNi18–10 sheet. Strength values were higher for 0° and 0° and lower for 0° . They also found significant variation in the

R-value during the forming process. You et al. [36] made macro and micro samples out of 361 L stainless steel along the rolling, transverse, normal, and inclined directions with similar results. The properties in the transverse direction were slightly stronger than in the rolling direction. Normal and inclined directions were much weaker. Eman et al. [37] used digital speckle correlation to look at the strain field in tension tests. In their results, stress-strain curves were not much different for the 0°, 45°, and 90° directions. Tardif and Kyriakides [38] tested seven tensile samples in increments of 15°, disk compression, and three plane strain samples at 0° , 45° , and 90° in Al6061-T6. The stress-strain curves were not significantly different. In a similar study, Chen et al. [39] used tension samples at seven different angles, plane strain at the three directions, and bulge test to study the behavior of Al2024-T3. Slightly higher strength was found with the 0° direction being the strongest and the 60° direction being the weakest. Corallo et al. [40] studied Ti6Al4V at high strain rates with samples at 7 angles. The strength was not very anisotropic with 45° and 60° samples having lower strength and 0° and 15° having higher strength. The R-value showed a trend of increasing from 0° to 45° and decreasing back from 45° to 90°. Marth et al. [41] studied post necking behavior of Al6061-T4 and AA5754-H111. Both metals showed slightly higher strength in the 0° than 45° and 90° directions. Rossi et al. [42] used DIC to study anisotropy in FP04 steel at 5 angles, 0°, 22.5°, 45°, 67.5°, and 90°. Stress strain curves were similar and R-values decreased as angle increased. Ghosal and Paul [43] found little change in strength in ferritic and dual phase steel along five angles of rolling direction.

In contrast to the extensive studies of anisotropy in constitutive behavior of sheet metals, anisotropy of localized necking and fracture has recently drawn attention in the literature. Abedini et al. [44] used butterfly shaped samples to create shear loading in ZEK 100 Mg alloy and DP 780 steel. ZEK 100 was anisotropic with high fracture strain at 90° and lower fracture strain at 45° and 135° to the rolling direction. The current study is different in that we are studying localized necking in uniaxial tension. Local fracture strain for the 0° and 45° directions were found to be higher than the 90° direction in high strength steel [37]. Failure strain was highest at 45° in ferritic steel and highest at 0° and 90° for DP steel in [43]. The literature review shows that anisotropy has been studied for constitutive behavior and to a limited degree for fracture, but less so for localized necking. Therefore, the goal of this research is to study the anisotropic behavior of the onset of localized necking, based on a geometry-based neck detection method.

The present study explores the maximum strain (strain limit) that a material can tolerate prior to experiencing localized necking in uniaxial tension. This investigation holds significant value in assessing the anisotropy impact on the mechanical characteristics and properties of the material. By evaluating the strain limits, a more comprehensive understanding of the materials' behavior and their response to deformations can be achieved. The approach employed in this study relies exclusively on the surface coordinates obtained through DIC measurements. In contrast to other neck detection approaches, this method does not use parameters such as strains, strain rates, and strain accelerations in its analysis. The strains (and strain path) will be assessed only after the localized neck detection algorithm has been completed by evaluating the surface profile and the geometry of the groove of the neck that subsequently develops.

A MATLAB analysis tool was developed for characterization of the anisotropic behavior of sheet metal subject to tension testing, with particular focus on material behavior during localized necking. The results of this analysis will be plotted and discussed in this paper. In section 2, the materials, data, and MATLAB analysis tool are described. In section 3, the results of stress-strain behavior, the spatial and temporal determination of the onset of localized neck, and anisotropic properties of the localized neck are discussed. Finally, conclusions and future work are discussed in section 4.

2. Materials and method

The experimental methods and setup are described in this section. First, the general DIC method that was used to gather the initial data is described. Then, the test sample and the position and strain data are described along with the structure of the data files. In the third section, the mathematical formulation that was developed to create the results is described.

2.1. Digital image correlation

DIC is an advanced, non-contact optical measurement technique that enables the analysis of deformations and strains in specimens subjected to external loads, as shown in Fig. 1. The recorded DIC data typically comprises time-sequential images capturing the specimen's deformation, accompanied by displacement and strain measurements obtained from different points across the surface of the object [45]. These measurements are acquired by examining digital images and monitoring patterns or markers on the specimen's surface as it undergoes deformation. This process allows for the creation of extensive 2D and 3D deformation vector fields and strain maps covering the entire observed area. By employing DIC technology, it becomes feasible to measure local strains precisely at a scale that encompasses an adequate number of grains, defining a Representative Volume Element (RVE) for the metal.

This facilitates the extraction of information regarding the local strains while macroscopic behaviors of the material can still be obtained.

2.2. Experimental DIC data

Publicly available DIC data was adopted for analysis in this research, from the Numisheet 2020 benchmark study on uniaxial tension testing, conducted by the NIST Center for Automotive Lightweighting [46]. This dataset encompasses the DIC data acquired from a set of 21 experiments conducted in the uniaxial tension test. The specimens were cut using an abrasive waterjet cutter, in accordance with the specifications illustrated in Fig. 2, utilizing DP980 sheet metals with a thickness of nominally 1.4 mm. These experiments were specifically performed using specimens exhibiting seven distinct orientations with respect to the RD: 0, 15, 30, 45, 60, 75, and 90° . Notably, the experiment was replicated three times for each particular orientation, utilizing three specimens cut at the same orientation.

In this study, analysis of the DIC camera images tracked 201 material points, which are evenly distributed at a distance of 0.25 mm from each other on the specimen's surface, running down the center line of the gauge area of the tensile specimen. The DIC analysis captures and records the information corresponding to the location and deformation of the points throughout the time of the deformation process. Each data set recorded at a specific instant of time generates a frame comprising



Fig. 1. Assessment of material deformation under tension utilizing a DIC. The setup features a testing machine that applies tensile force to the specimen, while the DIC camera system captures detailed deformation data. The resulting strain map highlights areas of strain concentration in various colors, processed by DIC analysis software.

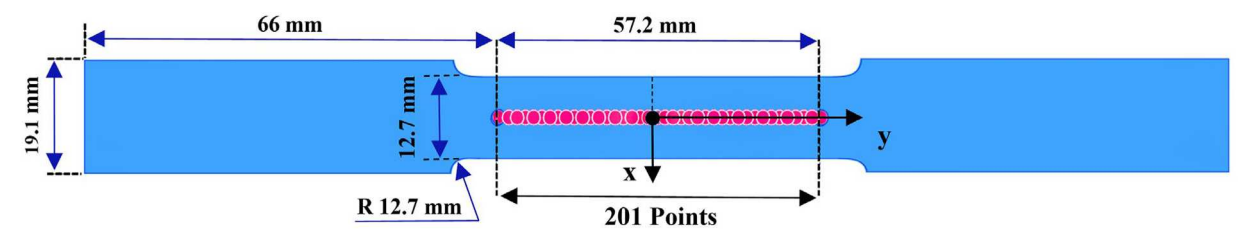


Fig. 2. Coordinate system and location of the points on the tensile specimen. The diagram illustrates the coordinate system with the y-axis running along the length of the specimen and the x-axis perpendicular to it. The origin of the coordinate system is located at the midpoint of the gauge length, which encompasses a total of 201 marked points along the y-axis. These points are used to measure strain distribution during tensile testing, enabling precise analysis of material behavior.

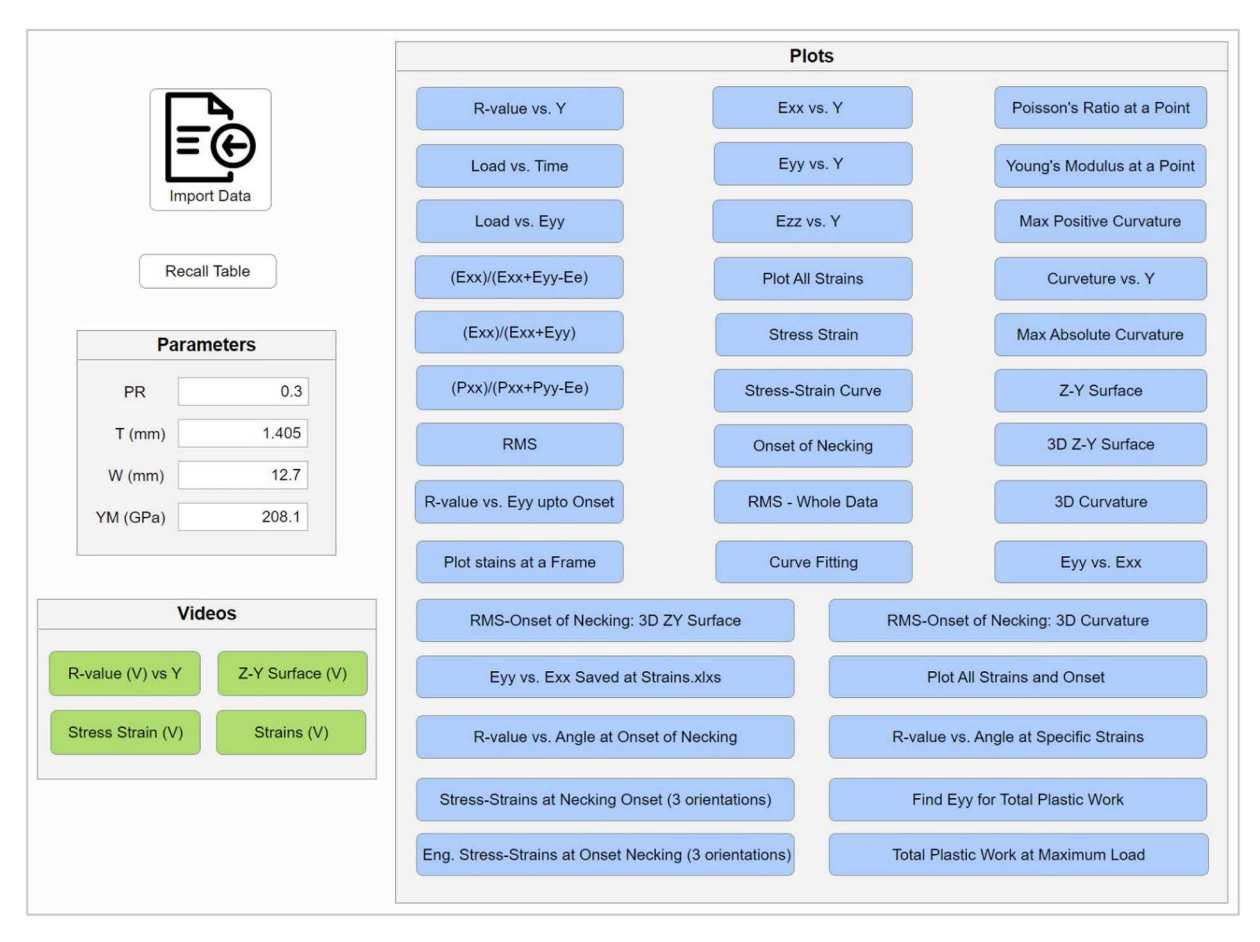


Fig. 3. The mathematical analysis tool developed to quantify anisotropy and detect the onset of necking in materials. It includes features for importing data, viewing key parameters, and providing various mathematical analyses and plotting options. The tool also offers video demonstrations for key analysis steps.

detailed data for all 201 material points. The frame-by-frame analysis reveals comprehensive details regarding the localized necking phenomenon, which enables the determination of the corresponding point on the forming limit curve (FLC) in the context of uniaxial tension. This analysis allows for precise characterization of the deformation behavior in the deformation zone, enabling engineers to make more reliable assessment of formability to more efficiently develop robust stamping tools for manufacture of sheet metal products, as well as improve necking and fracture prediction in product performance simulations to ensure stamped metal products meet or exceed design performance targets.

In the uniaxial tension test, the DIC system generates a set of recorded data with six columns, including x, y, z, ε_{xx} , ε_{yy} , and ε_{xy} for each of 201 material points running down the centerline of the test specimen, resulting in a total of $6 \times 201 = 1206$ columns of data for all the points evaluated on the specimen shown in Fig. 2. The x, y, and z coordinates of these 201 points provide accurate measurements of the displacement of each material point in the course of the uniaxial test and can be employed in localized neck detection through the curvature algorithm.

The set of 21 DIC data source files for the uniaxial tension of individual specimens follows a specific naming format designed for test identification and analytical control. For instance, based on this naming format, the name of all DP980 specimens subjected to uniaxial tension test starts with the character "U", as an indicator for the uniaxial tension at the beginning of a file name: U00FeDP980RiiTx.xxxWyy.yy.csv. The two-digit character "00" represents the angle of specimen orientation, replaced by one of the following orientations: 0, 15, 30, 45, 60, 75, or 90. The next two-character, "Fe," denotes the primary element of the metal, which is followed by the name of the material, which in the context of this study is DP980. The two-digit "ii" in Rii represents the

repeat index, identifying the identification of the specific specimen ID from the multiple tests of the same condition. The x.xxx in the Tx.xxx and yy.yy in the Wyy.yy reports the measured sheet thickness and width of the specimen in mm, respectively.

The CSV file also includes 11 extra columns beyond the initial 1206 columns provided by NIST Center for Automotive Lightweighting for the uniaxial tension test. Within the additional data columns, three particular columns are crucial for the analysis. Firstly, there are two columns that record the precise timing of the two snapshots captured by the two DIC cameras. Lastly, a column that specifies the corresponding load recorded at the same moment when each snapshot was triggered.

2.3. Mathematical analysis of data

As shown in Fig. 3, a mathematical MATLAB tool was developed to conduct advanced mathematical computations and numerical analysis on the DIC data. This mathematical tool enables precise and detailed data analysis for detection of the onset of localized neck and characterization of anisotropic properties of materials. This tool can be employed in studies where DIC data analysis plays a crucial role in understanding deformation behaviors and material properties. Through an initial analysis, the provided tool enables the extraction of Poisson's ratio and Young's modulus through preliminary analyses, strain values, as well as the specimen's thickness and gauge width, which collectively determine the cross-sectional area of the specimen. Then, these key parameters will be used as input data, along with the location of points, time, and strain values, to conduct further comprehensive data analyses.

The tool developed allows for uploading large DIC data files, automatically converting them into the appropriate tables and matrices required for each specific analysis. This capability eliminates the need

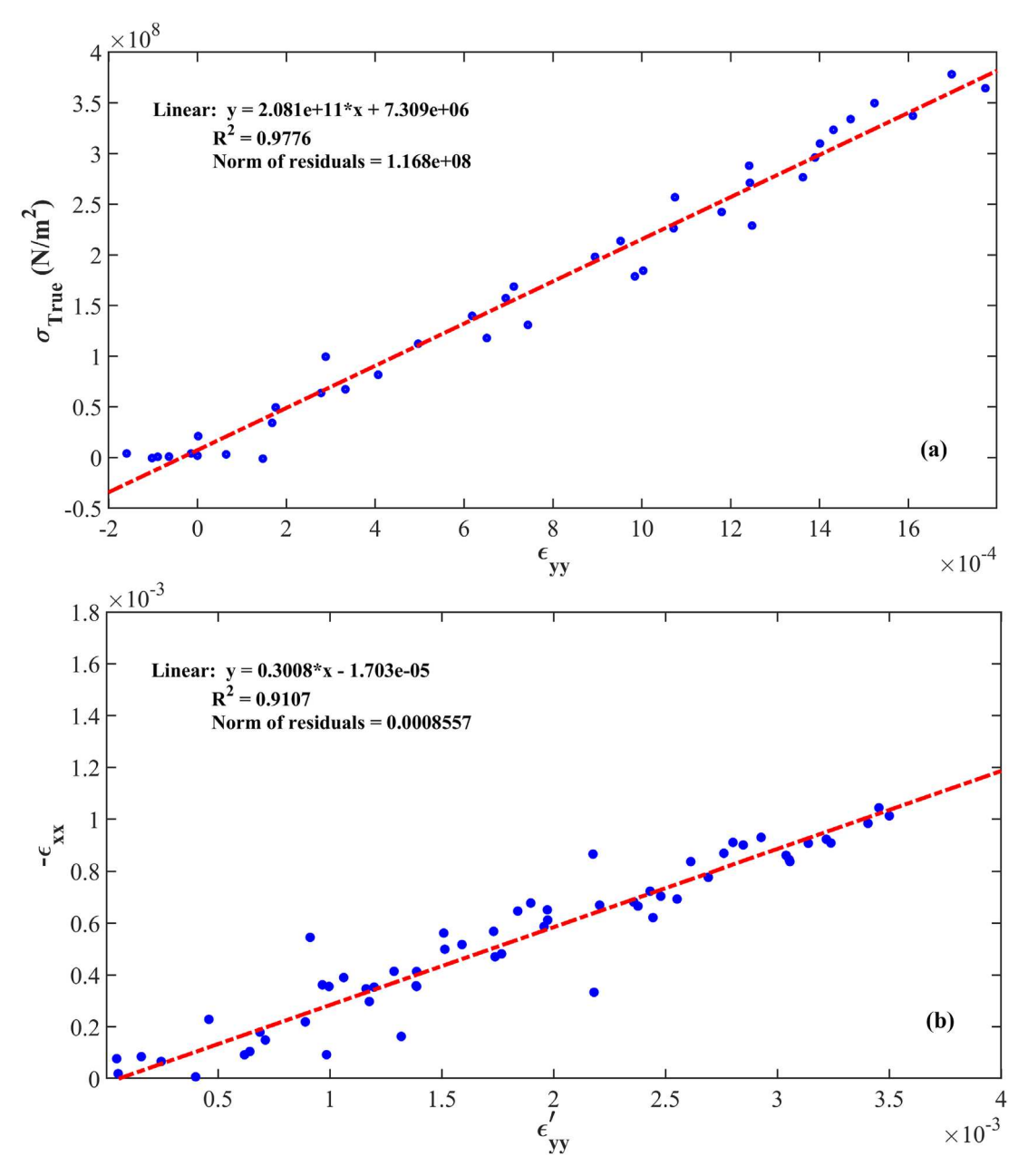


Fig. 4. Calculating Young's modulus and Poisson's ratio using DIC data recorded in the test file named U00FeDP980R01T1.405W12.7. The slope of the fitted line in the top and bottom figures represents Young's modulus and Poisson's ratio of the material, respectively.

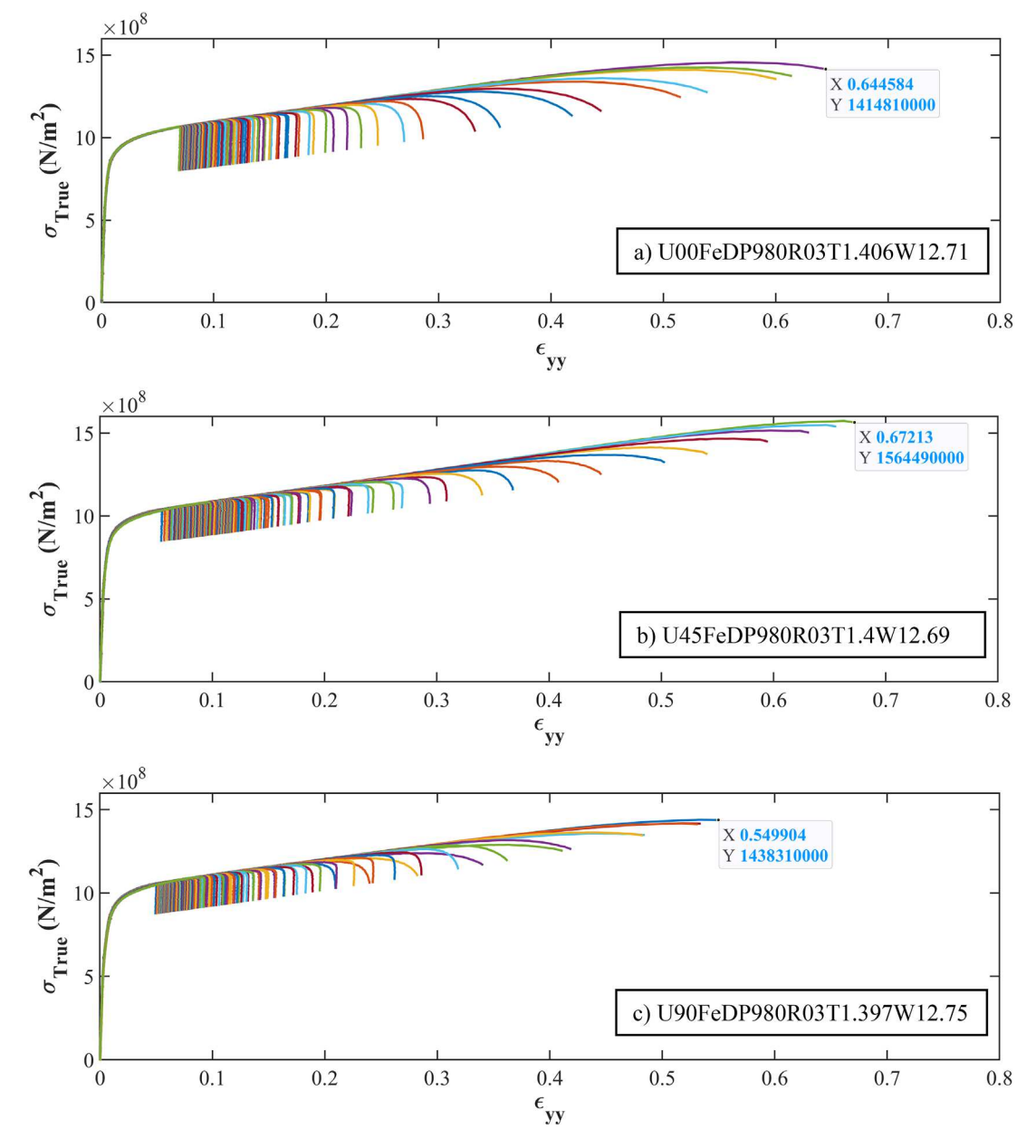


Fig. 5. True stress-strain curves for all material points on samples with a) zero, b) 45 and c) 90-degree with respect to the RD.

for manual data preparation and preprocessing stages. By automating all steps of the process, the tool significantly reduces the time and effort required to prepare the data for analysis and enables the work with large DIC datasets more effectively. The developed mathematical tool encompasses various code segments, including an import module specifically designed to import DIC data, along with parameter fields allowing the user to input crucial properties such as Young's modulus, Poisson's ratio, specimen thickness and gauge width. Furthermore, the tool comprises an analysis section that conducts mathematical analyses and calculations and generates results, and presents them through a variety of plots, aiding in the visual interpretation of the findings. Furthermore, this tool offers the capability of visualizing parameter development over time by creating dynamic movies, facilitating a deeper understanding of the data's temporal evolution for assessing surface profile, R-value, and strains in all three directions.

The R-value, also known as the Lankford coefficient or plastic strain ratio, is an important parameter in plastic deformation of sheet metals and offers a means of assessing how a metal alloy resists thinning. In

mathematical terms, it is defined by the ratio of the true plastic strainrate, $\varepsilon_{p,w}$, experienced across the width of a specimen pulled in uniaxial tension over the true plastic strain-rate through thickness, $\varepsilon_{p,t}$. For convenience, it is sometimes approximated in terms of the ratios of the total strain rates, $\varepsilon_w/\varepsilon_t$, and more often, in terms of the net strain in these two directions, $\varepsilon_w/\varepsilon_t$ at a specific longitudinal strain, usually defined at the limit of maximum load, using the following formula:

$$R = \frac{\dot{\varepsilon}_{p,w}}{\dot{\varepsilon}_{p,t}} \approx \frac{\dot{\varepsilon}_{w}}{\dot{\varepsilon}_{t}} \approx \frac{\varepsilon_{w}}{\varepsilon_{t}}$$
 (Eq. (1))

where $\dot{\varepsilon}_{p,w}$ and $\dot{\varepsilon}_{p,t}$ represent the rate of plastic strain along the width and thickness of the specimen, respectively. The first simplification of the Eq. (1) arises from the dominance of the magnitude of plastic strain over elastic strain beyond the yield point, and the second simplification is based on evident or assumed linearity of the strain path up to a strain level before localized (through-thickness) necking, a phenomenon elaborated upon in the results section. It is crucial to mention that for

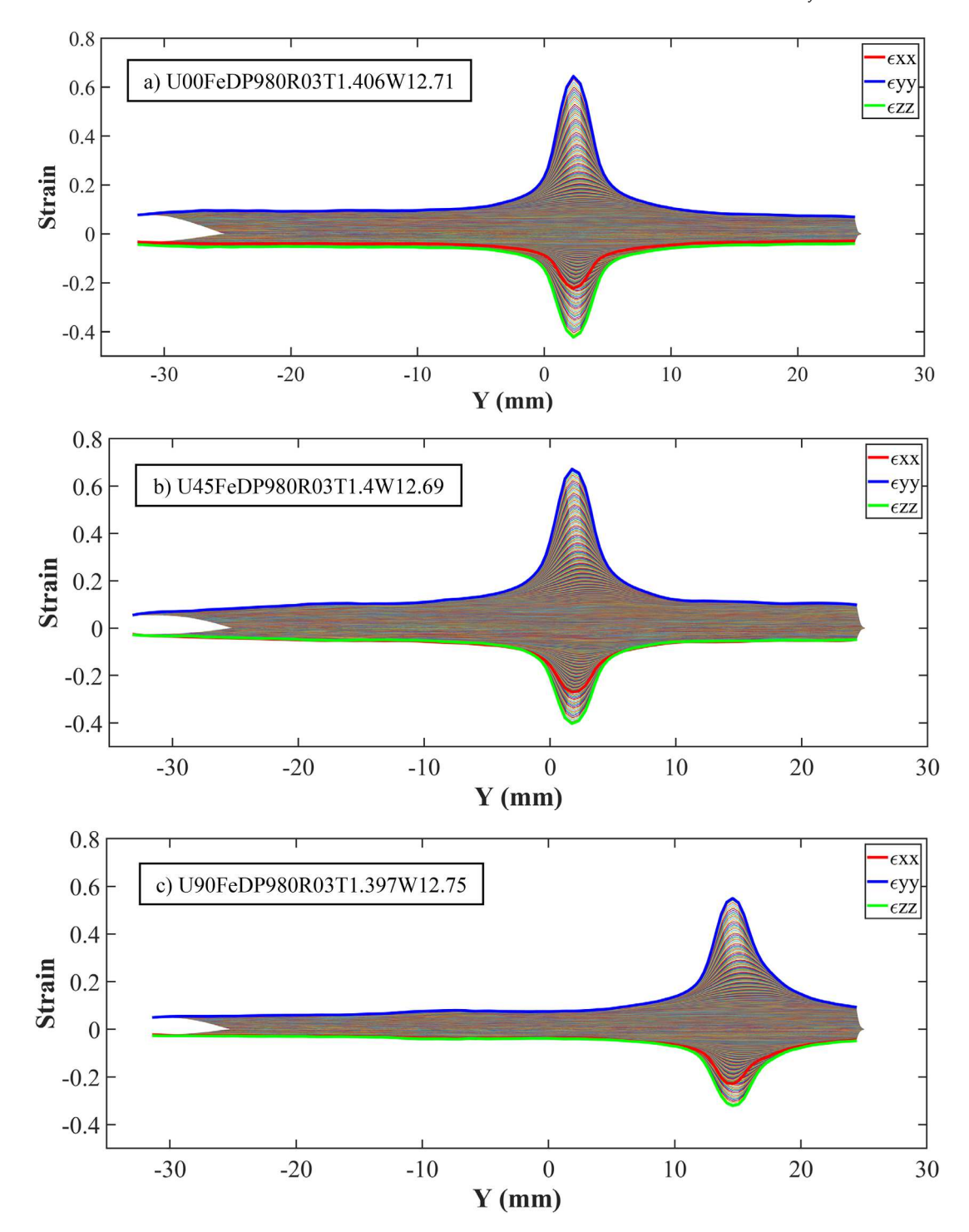


Fig. 6. Temporal strain curves for all material points on samples with a) zero, b) 45 and c) 90-degree with respect to the RD over the course of tensile testing.

high-precision analyses employing accurate technologies like DIC and the curvature approach, it becomes imperative to account for the effects of elastic dilatancy as follows:

$$\varepsilon_{xx} + \varepsilon_{yy} + \varepsilon_{zz} - \varepsilon_E = 0$$
 (Eq. (2))

$$\varepsilon_{zz} = \varepsilon_E - (\varepsilon_{xx} + \varepsilon_{yy})$$

where the term $\epsilon_{\chi\chi}+\epsilon_{yy}$ represents the magnitude of the thinning strain and:

$$\varepsilon_E = \varepsilon_{E xx} + \varepsilon_{E yy} + \varepsilon_{E zz} = \frac{Fe^{\varepsilon_{yy}}}{EA_0} (1 - 2v)$$
 (Eq. (3))

therefore,

$$\varepsilon_{zz} = \frac{Fe^{\varepsilon_{yy}}}{EA_0} (1 - 2v) - \varepsilon_{xx} - \varepsilon_{yy}$$
(Eq. (4))

in this equation, F is the applied force, E is the Young's modulus, and v is the Poisson's ratio. The calculation of the local stress is based on the assumption that the uniaxial load is distributed uniformly over the area of any plane through the specimen that is perpendicular to the axial

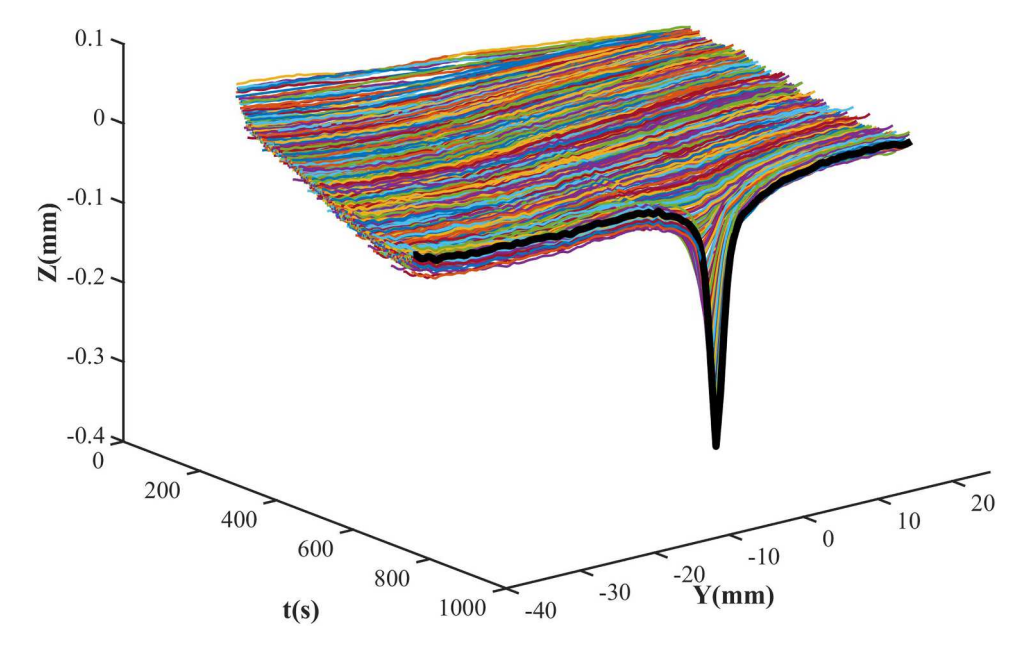


Fig. 7. Specimen's surface profile including all frames throughout the process (sample U00FeDP980R03T1.406W12.71). Each frame shows the location of the material points at a specific moment. The curves illustrate the evolution of the surface profile of the material points. The heavy black curve highlights the data from the final frame before the fracture occurred.

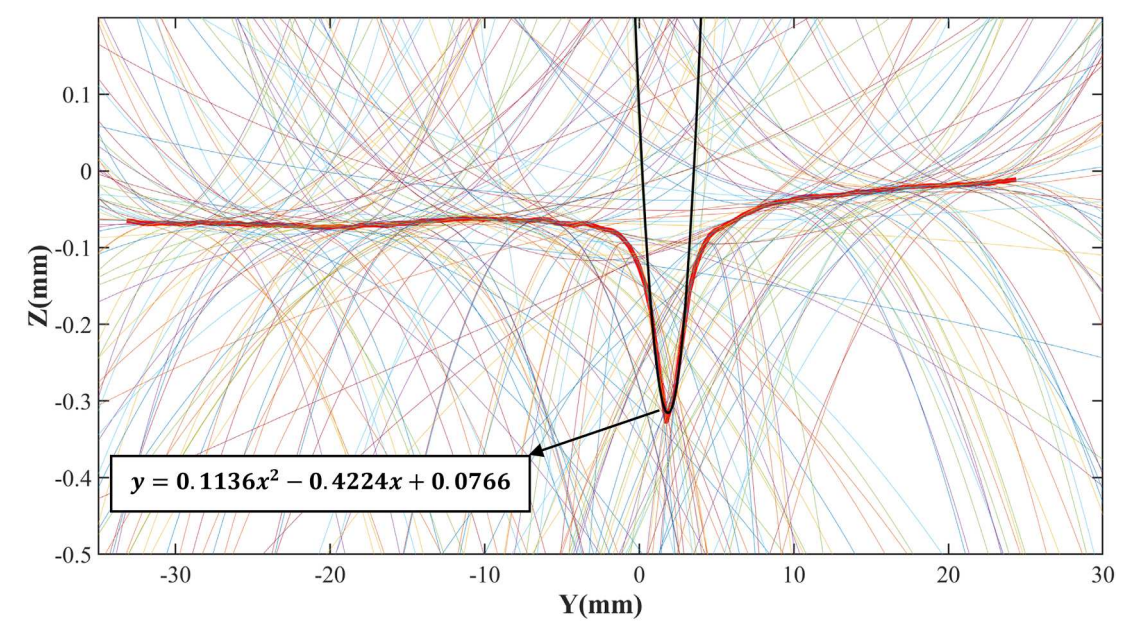


Fig. 8. Curve fitting on sample U45FeDP980R03T1.4W12.69. The local curvature of the material points on the specimen's surface is calculated by fitting a parabolic curve to five consecutive points within a frame, starting with the first point on the left. The curvature is determined at the third point of these five. For subsequent points, the curvature is obtained by fitting a parabola to a new set of five points, each shifted one point to the right.

load. The true stress can be derived from the engineering stress as follows:

$$\sigma_{true} = \frac{F}{A_i} = \frac{F}{w_i t_i} = \frac{F}{w_0 t_0} \exp \left(\varepsilon_{yy} - \frac{1 - 2v}{E} \sigma_{true} \right)$$
 (Eq. (5))

Young's modulus and Poisson's ratio are important factors that must be included in an analysis. To determine Young's modulus, an assessment focused on the beginning part of the true stress-strain curve. A linear regression analysis was applied to the dataset, resulting in a fitted line where the slope represents Young's modulus of the material. As shown in Fig. 4(a), there is a non-zero intercept, which is due to the error in establishing the material points in the first recorded image. This error is analogous to an error in the calibration of a strain gauge, which results in strain offset measurements in all subsequent frames. Removing the effects of this error in the entire frames, provides modified ε_{yy} strain values, represented as ε'_{yy} .

Poisson's ratio, which is a fundamental material property that quantifies the relationship between axial strain and lateral strain when a material is subjected to mechanical loading. To determine the Poisson's ratio, the values of $-\varepsilon_{xx}$ were plotted against ε_{yy}' for a random point on

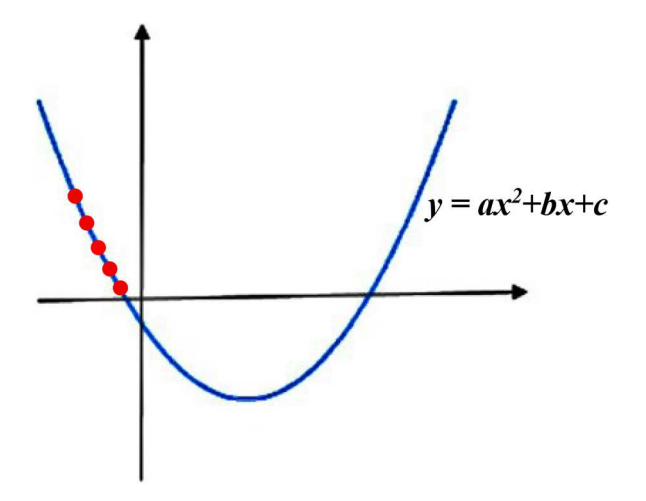


Fig. 9. A sample quadratic polynomial fitted to a set of material points. The red dots represent a sample set of 5 material points to which the quadratic equation $y = ax^2 + bx + c$ is fitted. These points can be located on either side of the curve or at any configuration, illustrating that the material points are not restricted to a specific format.

the specimen from the very beginning phase of deformation, within a strain range where ϵ'_{yy} remained below 3.5 \times 10⁻³. Subsequently, a linear regression line has been fitted to the dataset, with its slope indicating the value of Poisson's ratio, as shown in Fig. 4.

3. Results

In this section, the processed results from the DIC data are presented. First, the calculated stress-strain behavior of the material and the temporal progression of strain are given for all 201 data points along the length of the sample. Then, the spatial position and curvature information are presented in the description of the localized neck detection method. The third subsection presents the anisotropic properties in the localized necking region.

3.1. True stress-strain curves and strain path across the length of the sample

Fig. 5 displays the relationship between true stress and true major strain for each material point captured by the DIC camera, revealing notable variations in the total strain at different regions on the specimen. Therefore, the utilization of DIC technology provides clear evidence that the strain distribution throughout the entire length of the tensile specimen is non-uniform, even at strains below maximum load, where the average true strain based on a 50 mm extensometer is about 0.08 for this DP980. The evolution of the strains over the course of tensile testing for all points along the sample has been presented in Fig. 6. The heavy blue, red, and green curves represent the strains along the specimen's length, width, and thickness at the last frame before fracture, respectively. By employing DIC technology to assess material deformation under tension, a separation in the curves may occur at the end of the tensile testing, indicating the occurrence of the fracture in the specimen.

3.2. Detection of localized neck by spatial curvature profile

The localized neck detection procedure is developed based on the material points' local curvature on the surface profile. In this method, it is crucial to obtain precise information regarding the surface profile of the specimen, which requires eliminating the effects of surface textures caused by markers or paints used for the DIC analysis. Therefore, a corrective process is required to ensure that the subsequent analysis focuses on the true deformation behavior rather than being influenced by the surface textures. To address this issue, a preprocessing step is implemented to level all material points based on their deviations from an initial surface elevation, so that the z coordinate of all material points in the first frame are set to zero. By analyzing the deviations of each material point from the initial surface elevation, a reference level was established that removes the first order effects of surface and paint texture. The reference level provides a clear representation of the specimen's surface, devoid of any artifacts or irregularities introduced by surface textures, as can be observed in the first frame of the data presented in Fig. 7. Then the difference in the elevation of each material point is subtracted from all the recorded frames to remove the effects of surface textures throughout the process for each material point.

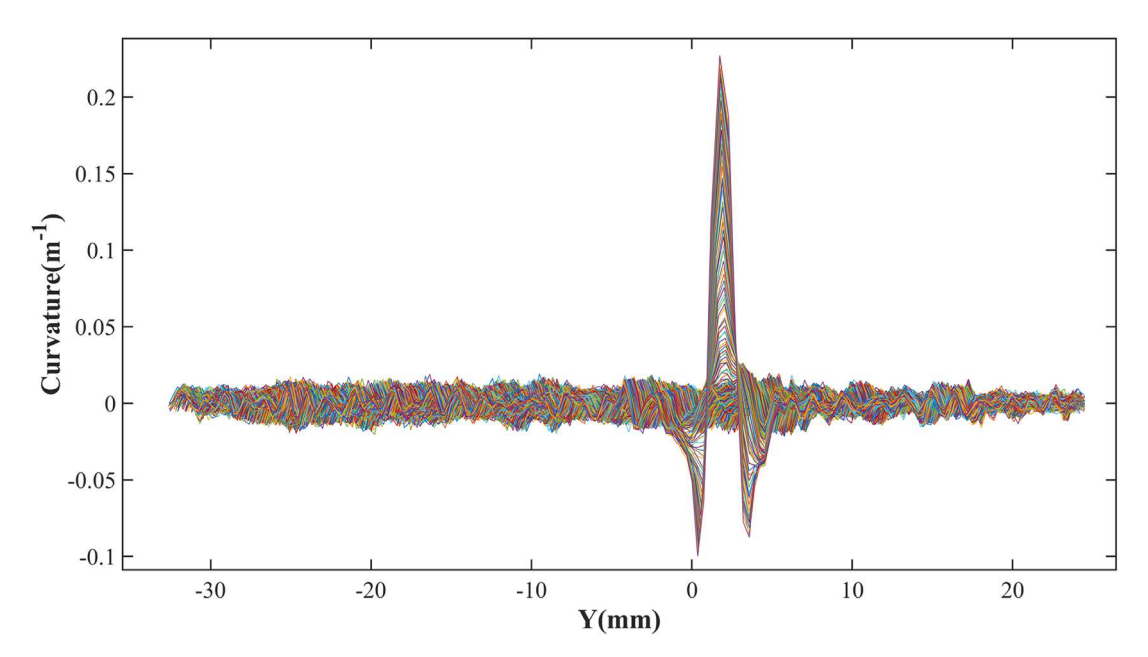


Fig. 10. Surface curvature development over the deformation process time for sample U45FeDP980R03T1.4W12.69. Initially, the curvature values of individual points show minor variations. As neck formation begins, significant changes in curvature occur, particularly in the diffuse neck region. This process is characterized by two major negative peaks flanking a large positive peak, distinctly identifying the onset and progression of localized neck formation.

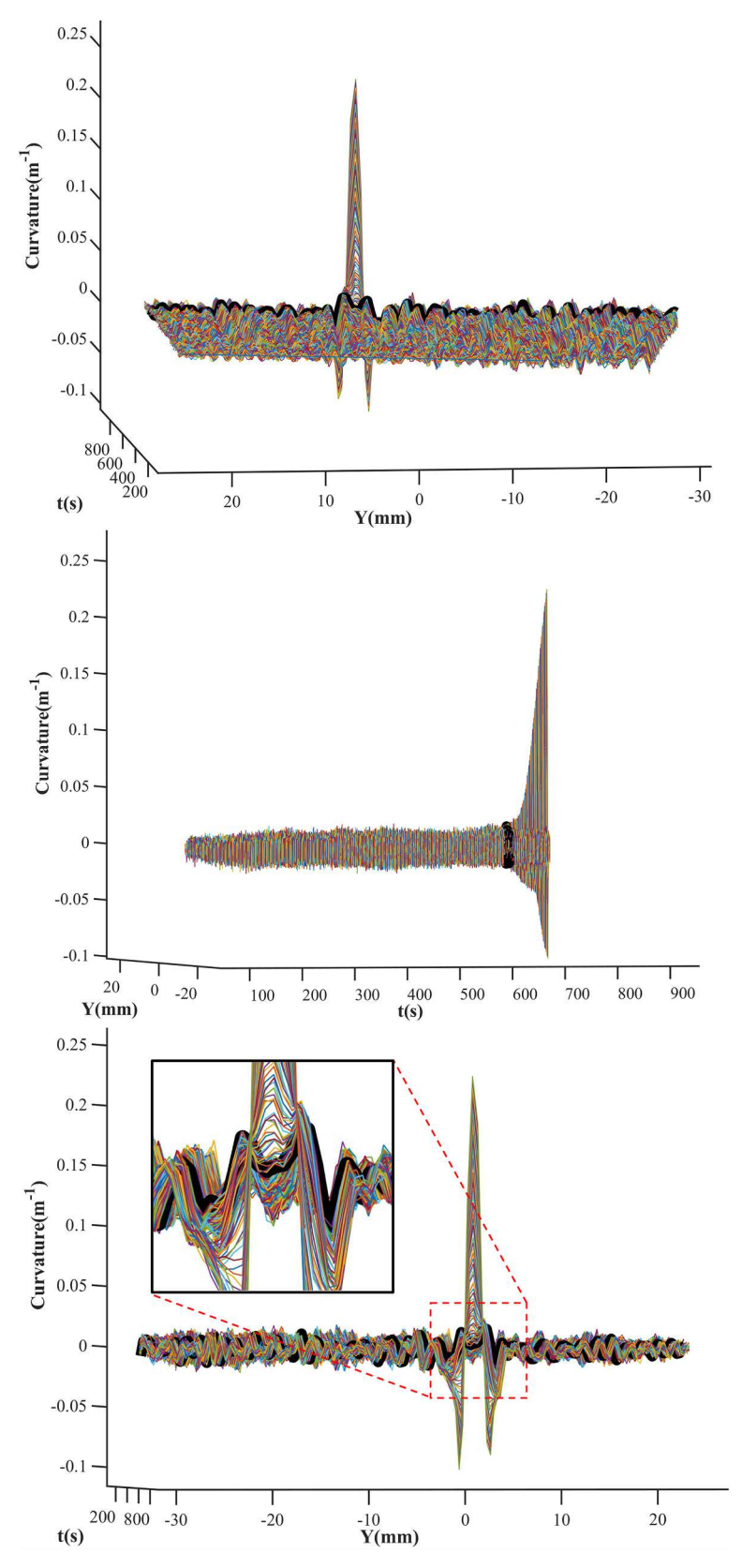


Fig. 11. Evolution of curvature profile for each material point throughout the process for sample U45FeDP980R03T1.4W12.69. Necking initiation is identified by computing the RMS of curvature values, excluding the neck region. The onset occurs when the curvature at the point with the highest value in the last frame first falls to or below the RMS curvature in the same frame. The frame marked by the thick black curve indicates the moment when this ratio drops to or below +1.0.

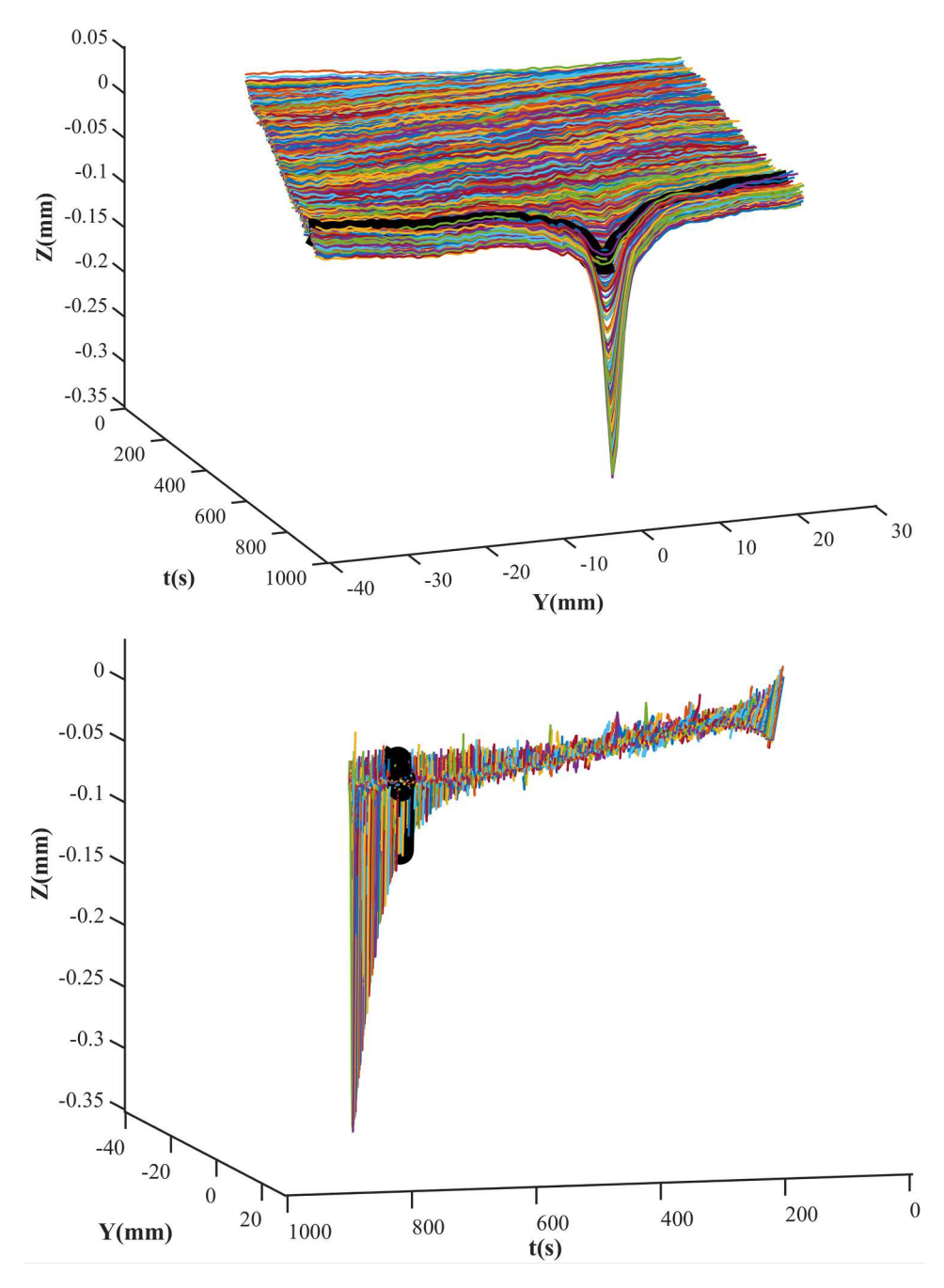


Fig. 12. Formation of localized neck on the surface profile of sample U45FeDP980R03T1.4W12.69. Initially, the surface profile is relatively flat. Diffuse necking significantly alters this profile, causing notable changes in the z-coordinate over an area approximately one to two times the width of the specimen. Localized necking introduces larger, more concentrated changes, which are superimposed on the effects of diffuse necking.

The heavy black curve depicted in Fig. 7 represents the data captured in the final image prior to the occurrence of the fracture. In this figure, the vertical scale is dramatically magnified compared to the horizontal scale to provide a highly detailed illustration of the vertical measurements of the surface profile. While the horizontal axis covers a span of 70 mm, the vertical axis span is 0.4 mm. This difference in the scales aims to effectively highlight and emphasize any variations or fluctuations in the surface profile within the vertical dimension. Therefore, the figure provides a magnified representation of the groove's depth within the surface profile, revealing a measurement of approximately 0.35 mm. This value accounts for around 25 % of the original sheet thickness, which was 1.406 mm.

The localized neck detection concept is focused on the local curvature of the material points located on the specimen's surface obtained by fitting a parabolic curve to 5 consecutive points in a given frame, starting with the first point on the left, and calculating the curvature at the center point of these 5 consecutive points, which is the third point in the list of points for that frame. The local curvature of the next center point (4th and later points) is defined by fitting to the 5 points obtained by dropping the first point from the list and adding the next consecutive point. As shown in Fig. 8, this process results in calculations of local curvatures at 197 points among the total of 201 points for each frame, starting at point 3 and ending at point 199.

Given that the curvature represents the inverse value of the radius of curvature, this relationship can be used to derive the following conclusions for every single quadratic polynomial, as presented in Fig. 9:

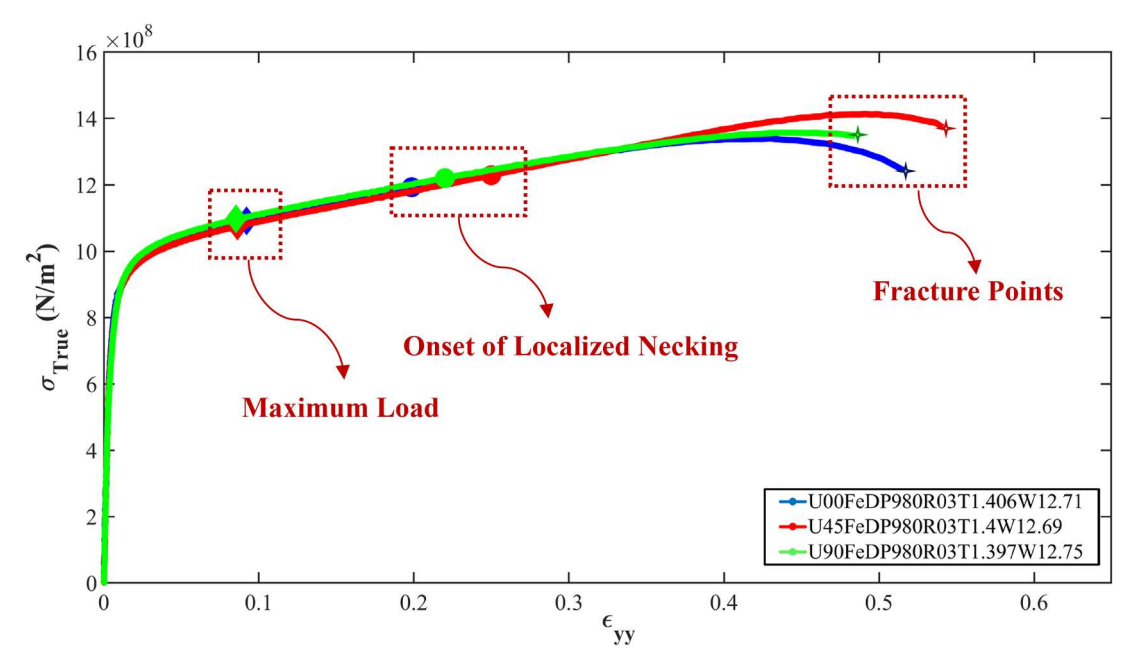


Fig. 13. True stress-strain curves of samples with 0, 45, and 90-degree with respect to the RD, highlighting critical points such as the maximum load, onset of localized necking, and fracture points.

$$k = \frac{1}{r} = \frac{|\ddot{y}|}{(1 + \ddot{y}^2)^{3/2}}$$
 (Eq. (6))

During the ongoing deformation of a specimen, the curvature values of individual points undergo slight changes. However, when the neck formation begins to take place, significant changes in curvature values occur in the diffuse neck region. The neck formation and significant changes in the curvature can be distinctly identified by observing two major negative value peaks accompanied by a large positive peak between them, as depicted in Fig. 10.

To effectively identify the initiation of necking based on curvature values, it is essential to extract the curvature fluctuations that arise throughout the process in the curvature profile. To achieve this objective, the root mean square (RMS) of curvature values for every material point has been computed across all recorded DIC data frames, excluding the curvature values within a region three times the thickness of the center of the neck groove. This exclusion is necessary because the material points within the region of the localized neck experience significant and abrupt fluctuations following the onset of localized neck. By excluding these points, we ensure that our measurements focus on the more stable and consistent regions, enabling us to capture the actual characteristics of necking behavior accurately. Following the discussed procedure, the RMS of curvature was calculated for each frame. The curvature in each frame was compared to the curvature at the point that shows the highest curvature value in the last frame. This comparison was performed frame by frame, moving backward in time. Onset of localized necking is defined to occur at the frame in which the curvature at this particular point first falls below the RMS curvature in the same

The proposed technique for neck detection centers around analyzing the local curvature values of the point exhibiting the highest positive curvature value in the final frame, which corresponds to the location at the bottom of the neck groove, if one is detected. First, the curvature of this identified point is divided by the calculated RMS of curvature values for other points in the last frame, and a neck is detected if the resulting ratio is significantly larger than 1. Furthermore, there must be two negative peaks on either side of the positive peaks, each lower in magnitude than the positive peak and located no more than approximately 2 times the sheet thickness away from the location of the positive

peak, corresponding to the valleys and two shoulders of the neck groove. The presence of two negative peaks and their specific locations are crucial characteristics defining the geometry of a groove emerging on the metal surface, corresponding to a localized neck.

By moving backward in time, the magnitude of the positive peak and two negative peaks decreases frame by frame. As previously described for detecting the onset of localized necking, repeating the ratio calculations at the reference point for each frame, moving backward in time, eventually causes this ratio to fall to or below +1.0 for the first time, which signifies the instant at which necking initiation occurs. The frame identified as the onset of localized necking is visually represented by a distinct and prominent thick black curve in curvature profile, as illustrated in Fig. 11. It should be noted that the precise instant of localized neck can be determined by interpolating the results measured at finite increments of time between the detected frame and the frame after that, in cases where the ratio has dropped to a value smaller than 1.

As previously mentioned, alterations in the curvature result in a distinct curvature pattern in the final frames, and all the samples will exhibit results that conform to that pattern. This pattern comprises a large positive peak in the center of two sharp negative curvature peaks, which are relatively smaller than the positive curvature peak. The distance between the negative peaks is a crucial parameter, and this is where the positive peak in curvature grows to a noticeable level, far beyond the background curvature, determined by the root mean square (RMS) of curvatures throughout the entire length of the specimen. The negative peaks represent the shoulders of the grooves, and the distance of these points (~3 mm in this case) is approximately two times the sheet thickness. In other words, the distance between the positive peak and an adjacent negative peak is approximately equivalent to the thickness of the sheet metal.

Prior to diffuse necking, the surface profile of the specimen is relatively flat reflecting a uniform and smooth specimen's surface. However, the initiation of diffuse necking has a significant impact on the surface profile of the specimen causing significant changes to the z coordinate spread over an area whose axial length is one to two times the specimen width. Later, as localized necking initiates, a much larger and more localized change occurs in the z coordinates that is superimposed on the changes caused by diffuse necking. Although localized necking dominates these changes as deformation continues, the detection of when

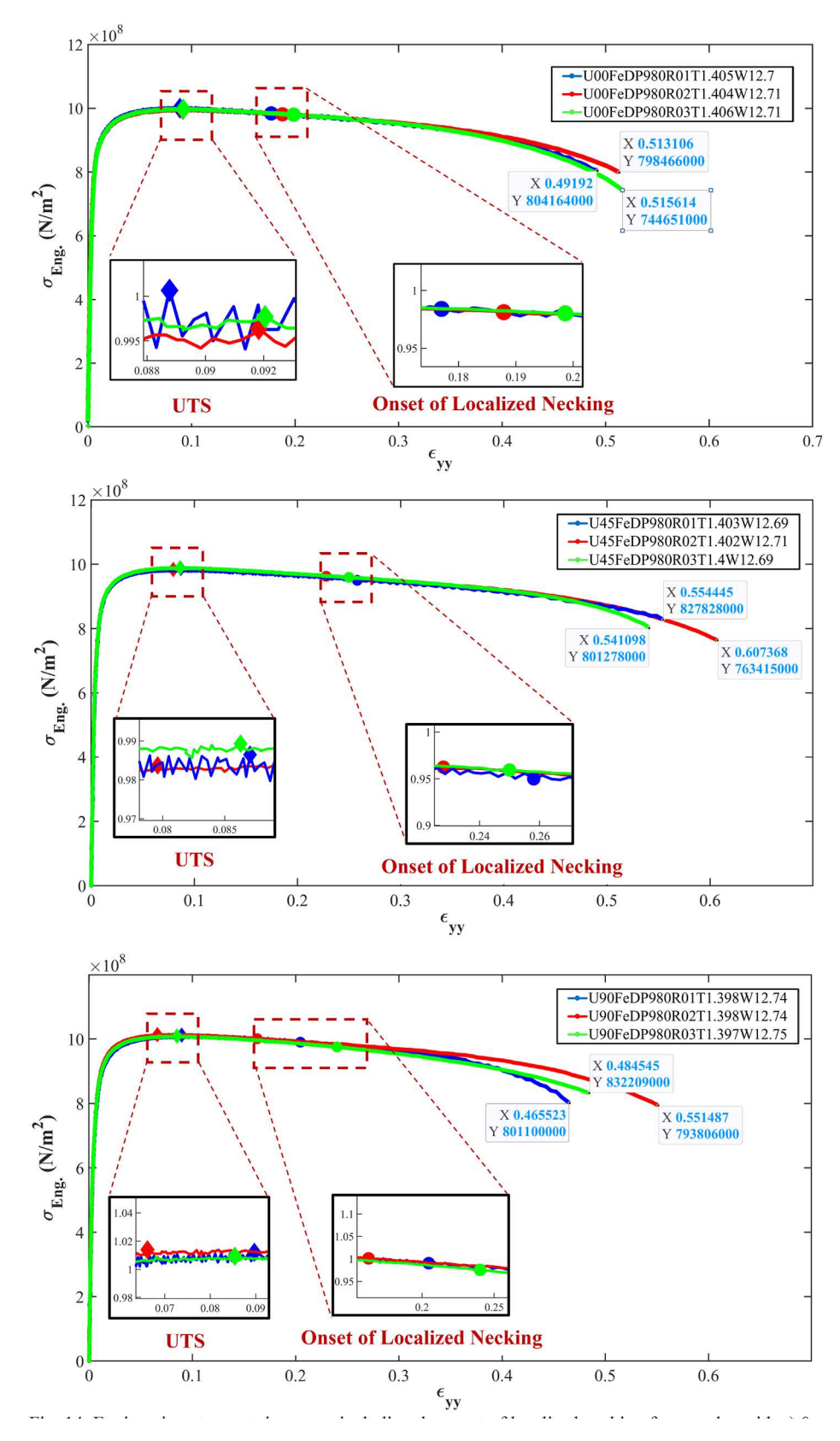


Fig. 14. Engineering stress strain curves including the onset of localized necking for samples with a) 0, b) 45, and c) 90-degree with respect to the RD. This figure shows that localized necking occurs between the UTS and fracture point, at a reasonable distance beyond the strain level at UTS.

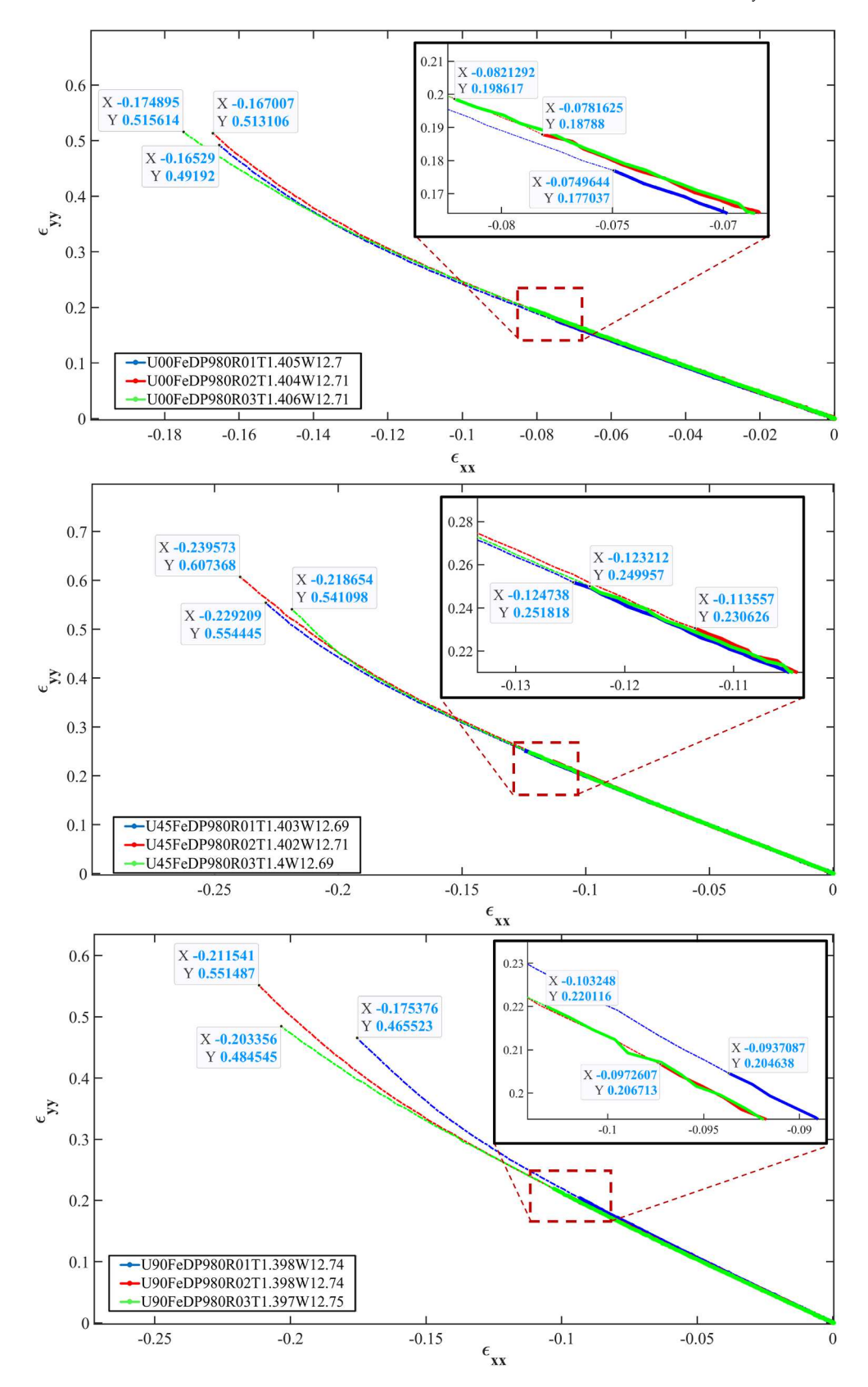


Fig. 15. Strain path of samples with different orientation with respect to the RD throughout the tensile test. The thick solid part of the curve represents material deformation before localized necking, while the dashed line shows the strain path after localized necking until fracture.

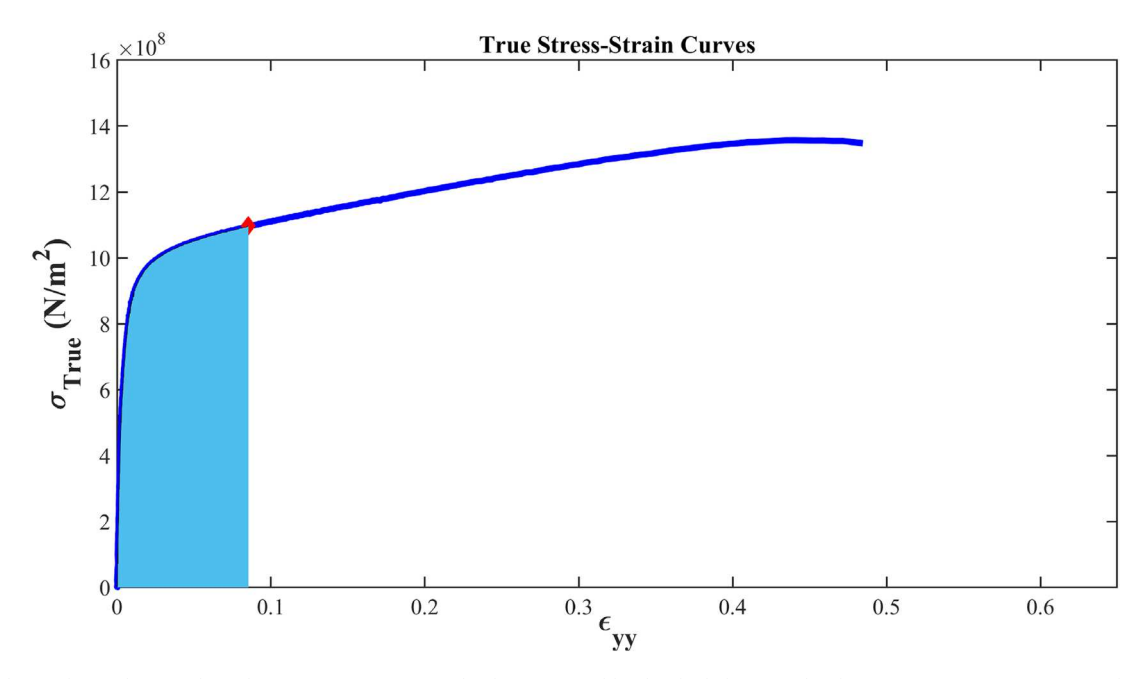


Fig. 16. Calculating the work-equivalent plastic strain at maximum load, represented by the shaded area under the true stress-strain curve up to the maximum load point. The average of these values for samples with zero-degree orientation with respect to the RD provides a reference that ensures a consistent level of plastic work across all samples, enabling accurate comparison of R-values, longitudinal strain, and thinning strain.

localization initiates, i.e., the decoupling of the effects caused by diffuse and localized necking, is not clear from the changes in Z-coordinate alone, as shown in Fig 12.

3.3. Anisotropic plastic behavior in the localized neck

The diffuse neck formation has a profound impact on the engineering stress-strain curve and corresponding values by introducing significant changes to the cross-sectional area of the specimen. In contrast, true stress is calculated taking into account the effect of the reduction in cross-section area; therefore, the true stress-strain curve will remain applicable beyond the formation of a diffuse neck. As the localized neck forms, strain becomes increasingly concentrated in this localized region, causing a consequential reduction in the cross-sectional area and an observable change in strain path. This phenomenon signifies a transition in the material's deformation mechanism, as the region undergoing necking exhibits higher level of strain in comparison to the surrounding regions. Fig. 13 exhibits the true stress-strain curves for three distinct samples characterized by orientations with respect to the RD of 0, 45, and 90°. The figure also highlights key points such as the locations of the maximum load, the initiation of localized necking, and the points of fracture.

The engineering stress-strain curves of the samples with zero, 45, and 90-degree orientations with respect to the RD for the material point located at the fracture location on the samples are presented in Fig. 14. The diamond shapes show the location of the ultimate tensile strength (UTS), known as the onset of the diffuse neck formation, where the material stretches significantly in the necked region while experiencing minimal deformation in other areas. In order to provide a better understanding of localized necking, the stress-strain curves have been marked with circles to indicate the particular locations where this phenomenon occurs. These circles serve as visual indicators, illustrating that the formation of localized necking takes place at a particular moment and location between the UTS and the fracture point.

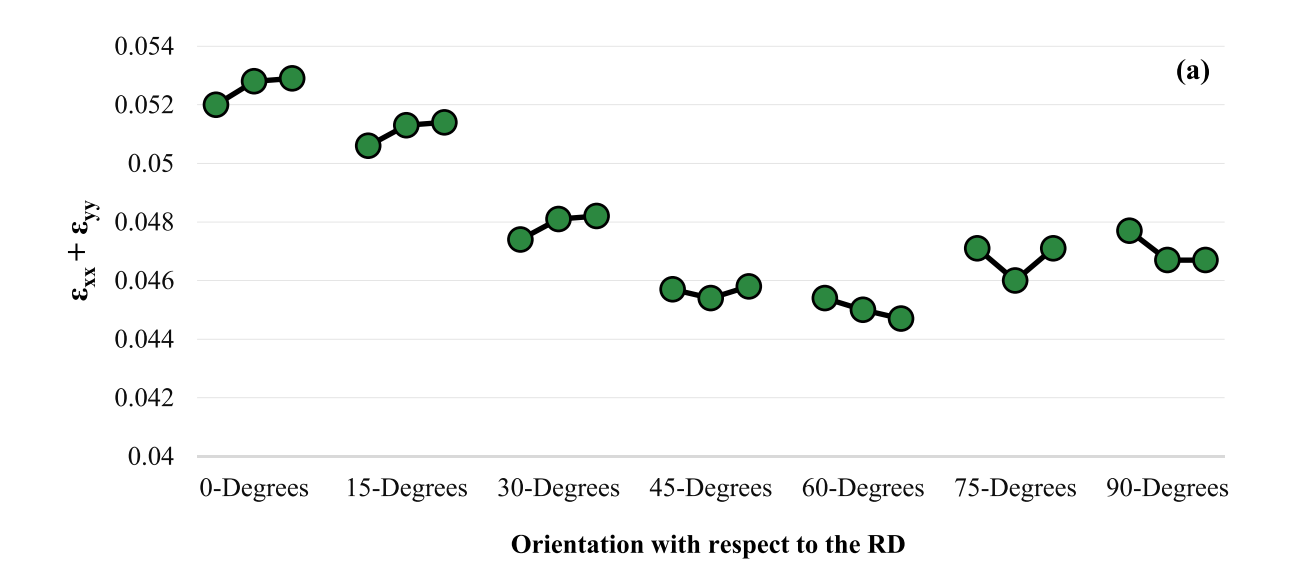
The proportional strain path exhibited by a material under uniaxial tension, where strains occur simultaneously in both the y and x directions, is called the material strain path and is illustrated in Fig. 15. The strain path of a material provides valuable insights into several

important aspects of its behavior such as deformation mechanisms, formability, and failure characteristics. The thick solid part of the curvature represents the deformation of the material prior to the formation of a localized neck, and the dashed line demonstrates the strain path afterward until the fracture. Notably, the strain path of three samples with the same orientations with respect to the RD follows the same nearly linear pattern before the localized neck formation and begins to slowly deviate from a straight line beyond this critical point.

To provide a meaningful comparison among specimens with different orientations with respect to the RD, examining parameters like R-values, longitudinal strain, and magnitude of thinning strain, it is essential to compute these values at a same level of plastic work for all samples. For this purpose, the work-equivalent plastic strain at the point of maximum load for the tests along the RD (0-degree) was determined by calculating the area under the stress-strain curve, as illustrated in Fig. 16. Then, the average of these values was adopted as the reference point, establishing a condition with the same level of plastic work for all the samples.

Fig. 17.a exhibits the maximum total strain $(\epsilon_{xx} + \epsilon_{yy})$ experienced by the material at the point with the same level of work-equivalent plastic strain, categorized based on different orientations with respect to the RD. Fig. 17.b shows the average values of $(\epsilon_{xx} + \epsilon_{yy})$, along with error bars demonstrating the standard deviation, for each orientation with respect to the RD, and the obtained patterns offer valuable insights into the impact of anisotropy on the material's forming limits. The obtained results revealed that samples produced with a 0-degree and 60-degree orientation with respect to the RD exhibit highest and lowest level of thinning strain levels compared to other orientations at the same level of work-equivalent plastic strain, respectively.

As discussed prior to summary of the anisotropy in localized necking limits, the R-value, also referred to as the plastic strain ratio, is another crucial parameter when it comes to the plastic deformation of sheet metals. The R-value provides a way to characterize the response of a metal alloy to deformation by measuring its ability to resist thinning during plastic flow. In this study, the evolution of the R-value throughout the process for all the evaluated points on the specimen has been presented in Fig. 18. The findings demonstrate a pattern wherein the R-value rapidly approaches a relatively stable state for all the points



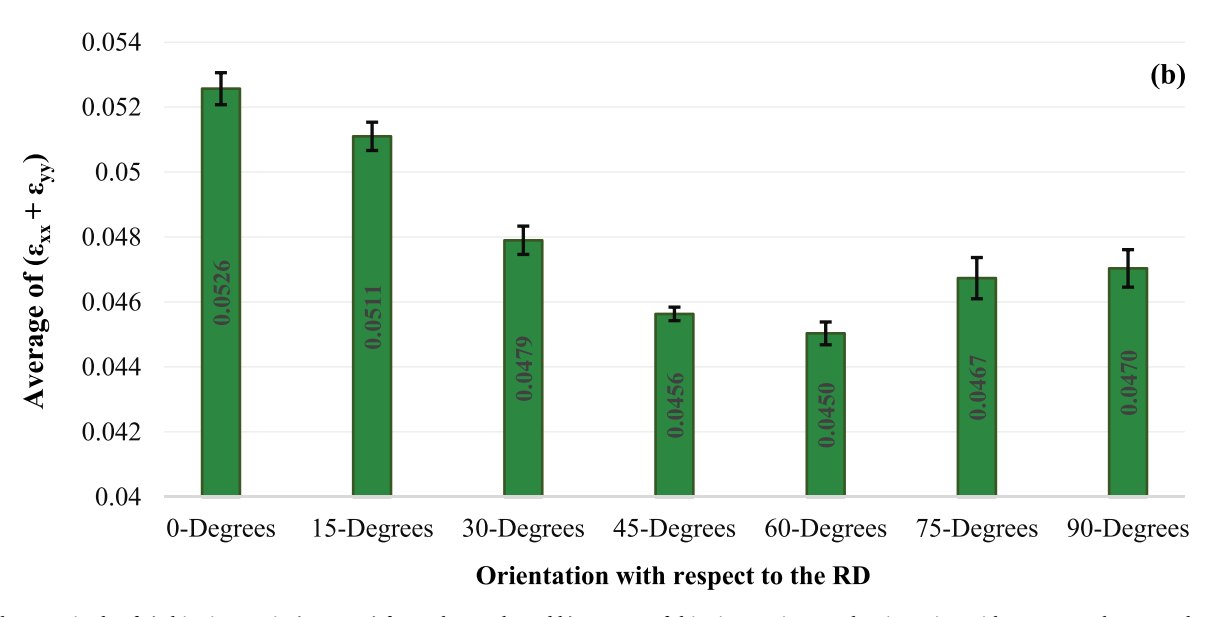


Fig. 17. The magnitude of a) thinning strain $(\epsilon_{xx} + \epsilon_{yy})$ for each sample and b) average of thinning strain at each orientation with respect to the RD at the same level of work-equivalent plastic strain.

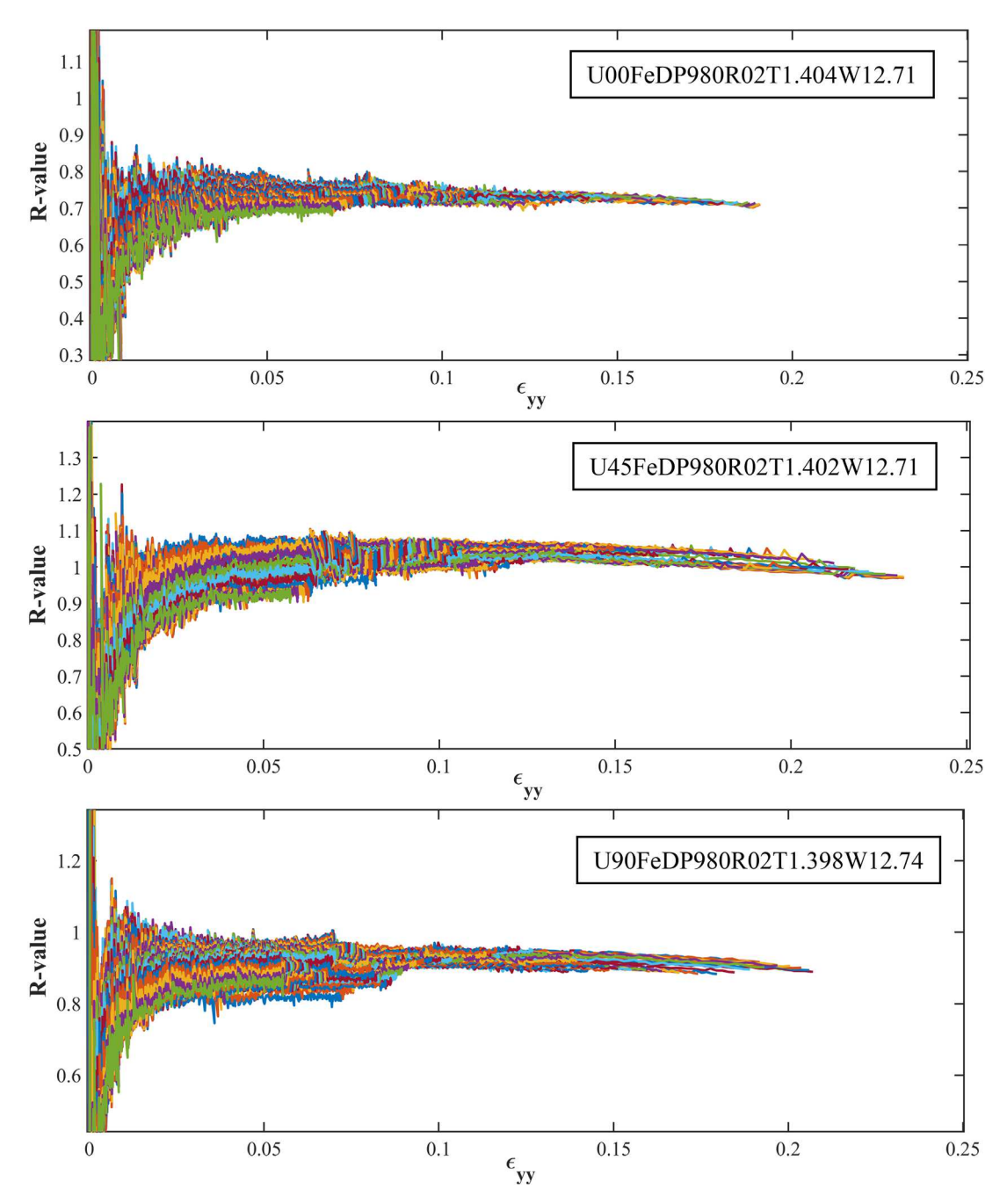


Fig. 18. R-value evolution for all the points throughout the tensile testing. After initial fluctuations at strain levels below 0.025, the R-value stabilizes. The fluctuations at lower strain values are mainly due to prominent DIC measurement errors, particularly when the two values defining the R-value ratio approach zero.

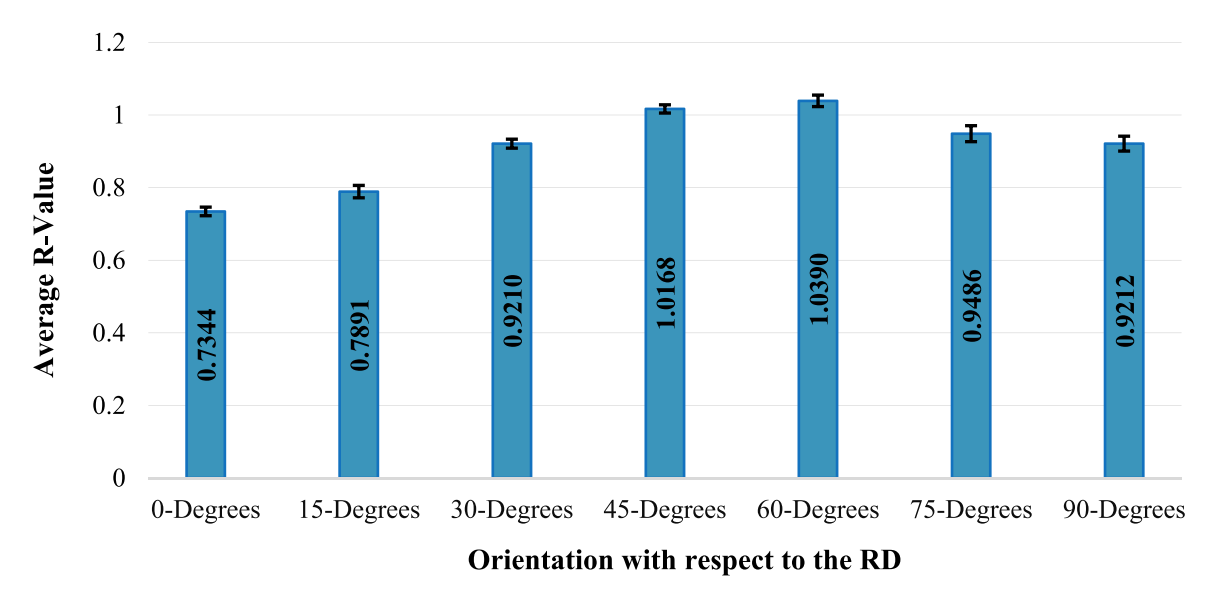


Fig. 19. The R-value for a) each sample and b) average R-value for specimens with the same orientation with respect to the RD at the same level of work-equivalent plastic strain.

after fluctuations at the initial stages of the process where the strain level is less than 0.025. The fluctuations observed at lower strain values primarily arise from DIC measurement errors being prominent, particularly as the two values defining the R-value ratio approach zero. However, it should be noted that slight variations may exist among the points due to their individual responses under plastic deformation. Furthermore, it is important to note that not all points undergo the highest levels of strain during the deformation process. As a result, many curves cease to show further growth, while only a few curves are able to reach higher strain values. Ultimately, the points within the diffuse neck zone experience significantly greater plastic strain following the same level of R-value up to the point where localized necking was initiated.

The R-value has been measured at the same level of work-equivalent plastic strain for specimens fabricated with different orientations with respect to the RD, as exhibited in Fig. 19. The R-value outcomes remain quite consistent among the three specimens produced with similar orientations with respect to the RD. The presented results revealed an increasing trend for R-value as the roll orientation increases from zero-degree to 60-degree, which offers the highest R-value, and then R-value decreases as the orientation increases. It should be noted that the minimum R-value was recorded at zero-degree with respect to the RD.

Similarly, the longitudinal strain values for each sample at the same level of plastic work level have been demonstrated in Fig. 20. The findings indicate that as the orientation with respect to the RD increases, the longitudinal strain exhibits a progressive increase, reaching its maximum level in specimens with a 30-degree orientation. Following this peak, there is a gradual descent, ultimately reaching its minimum value in specimens oriented at 90-degree.

Fig. 21 illustrates the relationship between the R-value and ($\epsilon_{xx} + \epsilon_{yy}$) at the same level of work-equivalent plastic strain, which reveals a negative linear correlation between these two parameters. The findings emphasize that specimens experiencing greater magnitude of thinning strain exhibit lower R-values, while conversely, those subjected to lower magnitude of thinning strain demonstrate higher R-values.

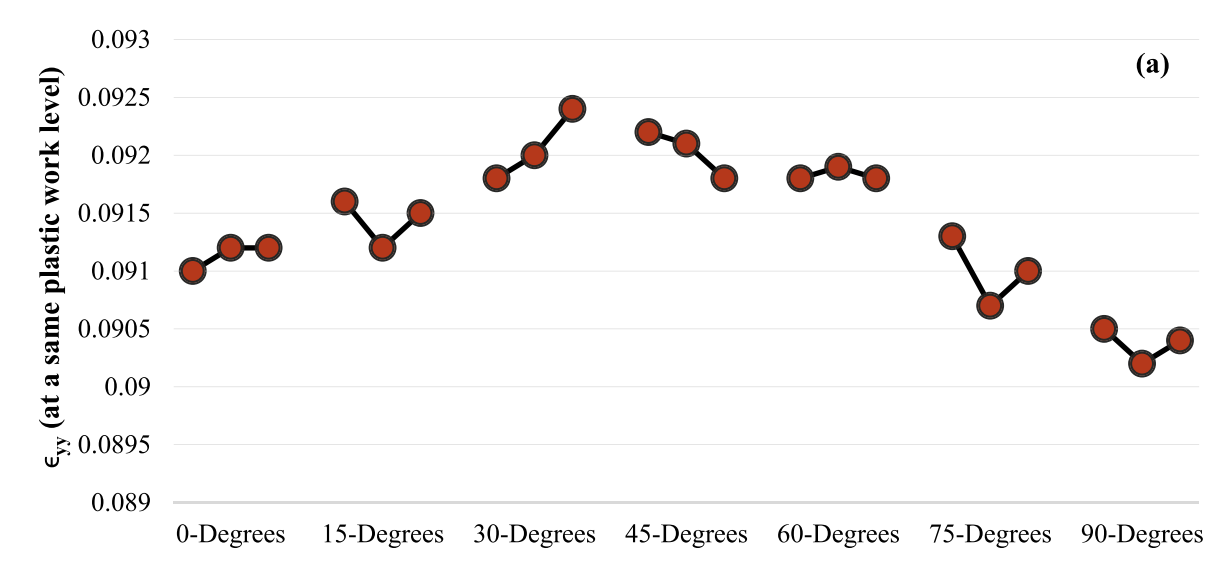
Fig. 22(a) illustrates and compares the longitudinal strain values experienced by the material point in each test that undergoes the maximum level of strain at a) the onset of localized necking, and b) the fracture point of the specimen for all orientations with respect to the RD. The obtained results exhibit that these particular material points experience the major portion of their total strain after the onset of localized necking.

It can be argued that the geometry-based approach presented in this

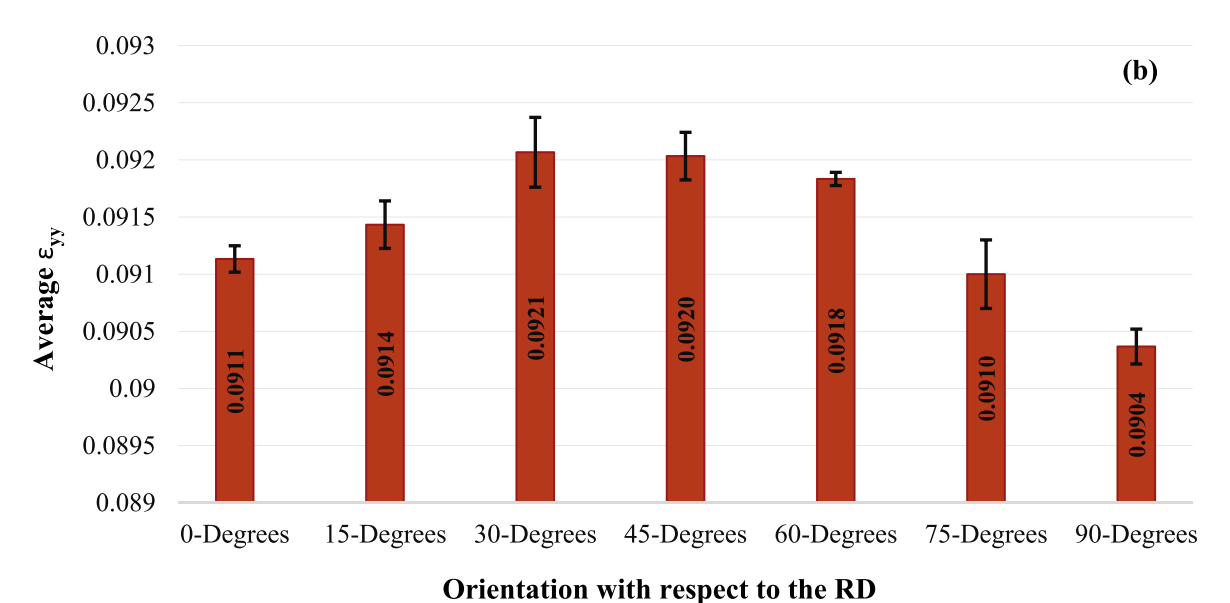
study has several advantages to be preferred over the strain-based methods as the presented technique can detect the onset of localized necking based on the DIC data using surface profile and the actual geometry of the groove, whereas some strain-based models may misinterpret strain localization caused by a diffuse neck to be evidence of a localized neck. A key issue found in many other neck detection methods is their inability to effectively distinguish between localized and diffuse necking. This limitation arises due to the fact that even diffuse necking induces inhomogeneity in the strain field and accelerates strain in areas where the thickness is at its minimum. For instance, suppose that the metal exhibits superplastic behavior without the formation of a localized neck. In such cases, most strain-based methods would mistakenly identify the presence of a localized neck due to the non-uniformity of strain resulting from the diffuse neck. It is mathematically impossible to distinguish the strain inhomogeneity caused by localized necking from that caused by diffuse necking; therefore, strain analysis alone cannot reliably detect the onset of localized necking, even for metal specimens in which a localized neck has been initiated. Due to this crucial reason, the DIC surface coordinates analysis approach has been employed in this study, which accurately determined the necking limits based on observation of the characteristics associated with a physical groove of appropriate dimensions associated with a localized neck. Nevertheless, as a means of verifying consistency and validating the results, the predicted location of localized necking has been examined on the engineering stress-strain curve, as shown in Fig. 15. This validation ensured that localized necking occurs after UTS, in a region near the upper end of the final drop in load prior to fracture.

4. Conclusion and future research direction

This study involved comprehensive advanced mathematical analyses of DIC data obtained from the uniaxial tension test to examine the impact of material anisotropy on various mechanical properties and behaviors. For this purpose, a MATLAB mathematical tool was developed to analyze DIC data of tensile tests of DP980, providing precise insights into localized neck detection and material anisotropy characterization using the curvature method. The introduced curvature technique employs the specimen's surface profile and groove geometry to identify localized necking, circumventing the drawbacks of strain-based analyses in discerning between localized and diffuse necking. The obtained results revealed that the formation of localized necking takes place within the process of non-uniform plastic deformation, located



Orientation with respect to the RD



Orientation with respect to the KD

Fig. 20. a) The longitudinal strain for each sample and b) average longitudinal strains for specimens with the same orientation with respect to the RD at the same level of work-equivalent plastic strain.

between the ultimate tensile strength and the fracture point. The negative peaks represent the shoulders of the grooves, and the distance of these points (\sim 3 mm in this case) is approximately two times the sheet thickness. In other words, the distance between the positive peak and an adjacent negative peak is approximately equivalent to the thickness of the sheet metal.

Although the limited sample size in this study may not provide definitive conclusions about the effects of material anisotropy, the results provided valuable insights, showing that a 30-degree orientation with respect to the RD leads to higher total strain levels during necking initiation. These findings contribute to the understanding of how anisotropy affects a material's deformation limits and fracture behavior. Moreover, the results revealed that the R-value initially fluctuates but eventually settles into a relatively stable state for most points; however,

variations in their values were observed at the initial stages of the test. The fluctuations observed at lower strain values can mainly be attributed to the dominance of DIC measurement errors, particularly as the two values defining the ratio of the R-value approach zero. Additionally, not all points experience the highest strain levels during deformation, particularly those outside the diffuse neck zone. Consequently, many curves stop showing further growth, while only a few points reach higher strain levels.

The result of strain path for the specimens with the same orientations with respect to the RD showed almost the same pattern up to the localized necking; however, a gradual divergence became noticeable beyond this point. As long as the strain path remains linear, it indicates that the stress state remains uniaxial, and there are no significant alterations in the microstructure that could impact R-values. Significant

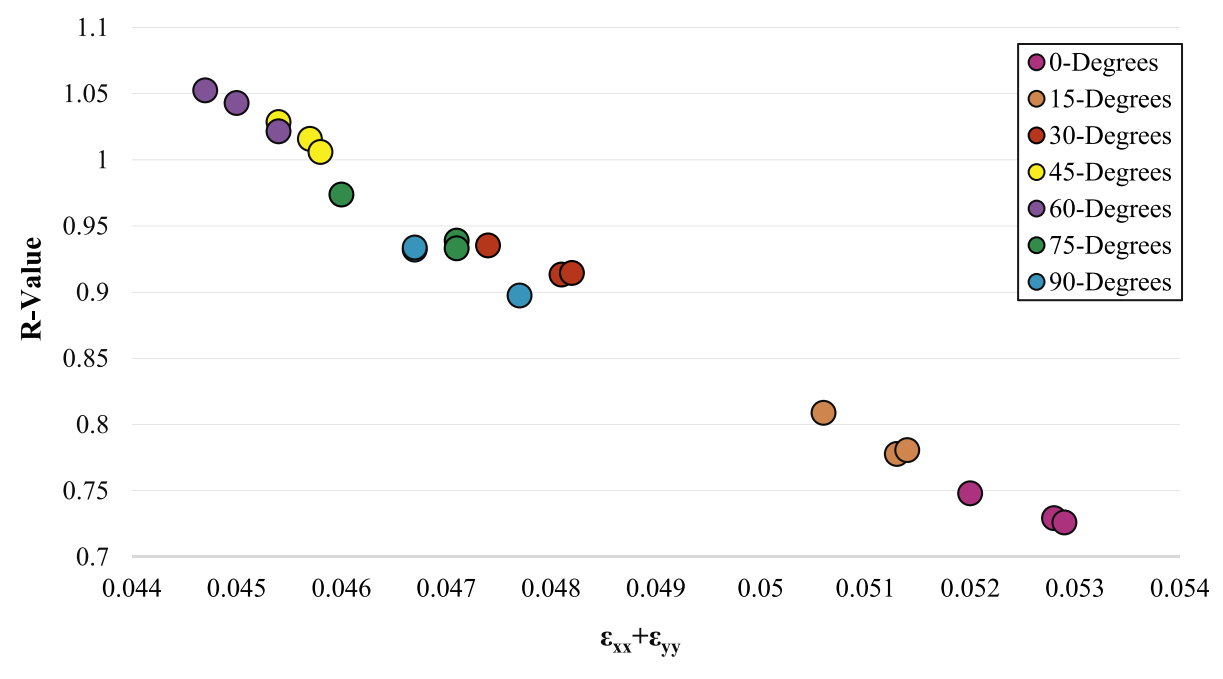


Fig. 21. R-value vs. the magnitude of thinning strain for each specimen at the same level of work-equivalent plastic strain.

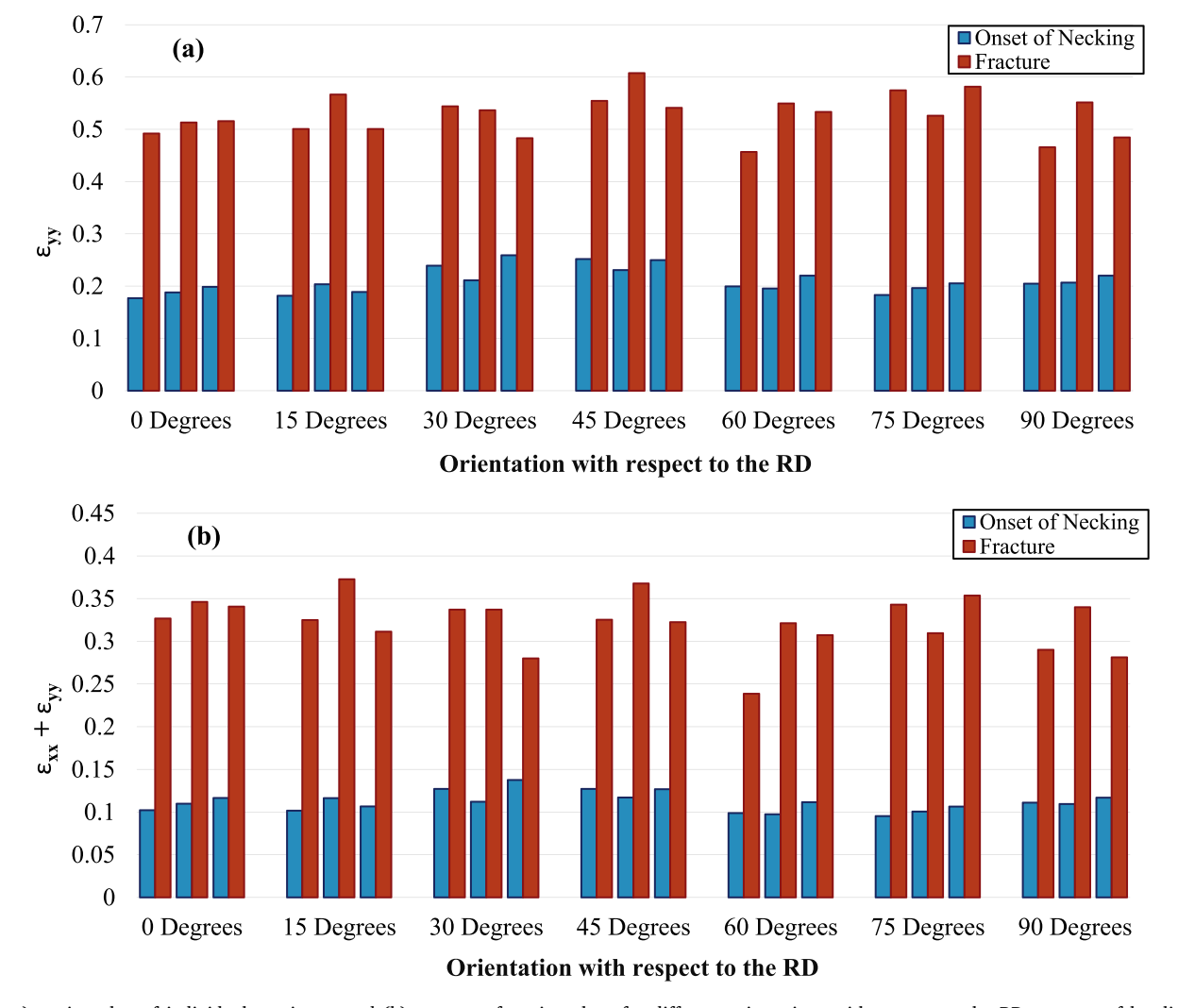


Fig. 22. a) strain value of individual specimens and (b) average of strain values for different orientations with respect to the RD at onset of localized neck and fracture.

divergence in the strain path became evident only after the onset of localized necking. Moreover, the obtained R-values at the same level of work-equivalent plastic strain in specimens with different orientations with respect to the RD revealed a consistent increase in R-value from zero-degree up to a 60-degree orientation with respect to the RD, followed by a decrease with further orientation increase. Additionally, the results revealed a negative linear relationship between the R-value and the magnitude of thinning strain across all the specimens.

CRediT authorship contribution statement

Ebrahim Seidi: Writing – review & editing, Writing – original draft, Visualization, Validation, Software, Methodology, Investigation, Formal analysis, Data curation, Conceptualization. Scott F. Miller: Writing – review & editing, Writing – original draft, Investigation, Funding acquisition, Methodology. Farnaz Kaviari: Software, Formal analysis, Data curation. Lu Huang: Writing – review & editing, Investigation. Thomas B. Stoughton: Writing – review & editing, Supervision, Methodology, Investigation, Conceptualization, Validation.

Declaration of competing interest

The authors declare that they have no known competing financial interests or personal relationships that could have appeared to influence the work reported in this paper.

Acknowledgments

This investigation was supported by NSF CMMI grant # 1763147, Office of Naval Research award # N000142112861, and General Motors.

Data availability

The data is publicly available at: https://www.tms.org/portal/downloads/meetings/2020/numisheet2020/MaterialData SourceFiles.zip.

References

- Park N, Stoughton TB, Yoon JW. A new approach for fracture prediction considering general anisotropy of metal sheets. Int J Plast 2020;124:199–225.
- [2] Hwang JK. Revealing the small post-necking elongation in twinning-induced plasticity steels. J. Mater. Sci. 2020;55:8285–302.
- [3] Fang S, Zheng X, Zheng G, Zhang B, Guo B, Yang L. A New and Direct R-Value Measurement Method of Sheet Metal Based on Multi-Camera DIC System. Metals. (Basel) 2021;11:1401. https://doi.org/10.3390/met11091401.
- [4] Nguyen VT, Kwon SJ, Kwon OH, Kim YS. Mechanical Properties Identification of Sheet Metals by 2D-Image Correlation Method. Proceedia Engineering 2017;184: 381–9.
- [5] Wang, Y.H., Jiang, J.H., Wanintrudal, C., Du, C., Zhou, D., Smith, L.M., and Yang, L.X., 2010, "Whole Field Sheet-Metal Tensile Test Using Digital Image Correlation, Experimental Techniques," 34(2), pp. 54–59.
- [6] Song Y, Green DE, Rose A. Investigation of various necking criteria for sheet metal formability analysis using digital image strain data. In J Mater Forming 2020;13: 1015–24.
- [7] Xie X, Li J, Sia B, Bai T, Siebert T, Yang L. An experimental validation of volume conservation assumption for aluminum alloy sheet metal using digital image correlation method. J Strain Anal 2017;52(1):24–9.
- [8] Romanowicz PJ, Szybinski B, Wygoda M. Application of DIC Method in the Analysis of Stress Concentration and Plastic Zone Development Problems. Materials, 13 2020:3460. https://doi.org/10.3390/ma13163460.
- [9] Martinez-Donaire AJ, Garcia-Lomas FJ, Vallellano C. New approaches to detect the onset of localised necking in sheets under through-thickness strain gradients. Mater Design 2014;57:135–45.
- [10] Li J, Yang G, Siebert T, Shi MF, Yang L. A method of the direct measurement of the true stress-strain curve over a large strain range using multi-camera digital image correlation. Optics lasers in engineering 2018;107:194–201.

- [11] Rossi M, Cortese L, Genovese K, Lattanzi A, Nalli F, Pierron F. Evaluation of Volume Deformation from Surface DIC Measurements. Exp. Mech. 2017;58: 1181–94.
- [12] Savic V, Hector Jr LG, Fekete JR. Digital Image Correlation Study of Plastic Deformation and Fracture in Fully Martensitic Steels. Exp. Mech. 2010;50:99–110.
- [13] Bourdin F, Stinville JC, Echlin MP, Callahan PG, Lenthe WC, Torbet CJ, Texier D, Bridier F, Cormier J, Villechaise P, Pollock TM, Valle V. Measurements of plastic localization by heaviside-digital image correlation. Acta Mater. 2018;157:307–25.
- [14] Zheng Q, Mashiwa N, Furushima T. Evaluation of large plastic deformation for metals by a non-contacting technique using digital image correlation with laser speckles. Materials and Design 2020;191:108626.
- [15] Zhu F, Bai P, Zhang J, Lei D, He X. Measurement of true stress-strain curves and evolution of plastic zone of low carbon steel under uniaxial tension using digital image correlation. Opt. Lasers. Eng. 2015;65:81–8.
- [16] Jordan B, Grolleau V, Mohr D. Using surround DIC to extract true stress-strain curve from uniaxial tension experiments. Int. J. Solids. Struct. 2023;268:112171.
- [17] Gu GH, Ahn SY, Kim Y, Seo MH, Kim HS. Determining reliable wide-strain-range equivalent stress-strain curves using 3D digital image correlation. J. Mater. Res. Technol. 2022;19:2822–30.
- [18] Iadicola MA. Uncertainties of Digital Image Correlation Due to Pattern Degradation at Large Strain. In: Jin H, Yoshida S, Lamberti L, Lin MT, editors. Conference Proceedings of the Society for Experimental Mechanics Series. 3. Cham: Springer; 2016.
- [19] Reu PL, Toussaint E, Jones E, Bruck HA, Iadicola M, Balcaen R, Turner DZ, Siebert T, Lava P, Simonsen M. DIC Challenge: developing Images and Guidelines for Evaluating Accuracy and Resolution of 2D Analyses. Exp. Mech. 2018;58: 1067–99.
- [20] Min J, Stoughton TB, Carsley JE, Lin J. A Method of Detecting the Onset of Localized Necking Based on Surface Geometry Measurements. Exp. Mech. 2017;57: 521–35.
- [21] Min J, Stoughton TB, Carsley JE, Lin J. An improved curvature method of detecting the onset of localized necking in Marciniak tests and its extension to Nakazima tests. Int. J. Mech. Sci. 2017;123:238–52.
- [22] Stoughton TB, Min JY, Carsley JE. Application of DIC techniques to detect onset of necking and fracture in uniaxial and bulge tests. Journal of Physics: Conference Series 2017;896(1):012108.
- [23] ISO/DIS 12004-2:2008. Metallic materials sheet and strip determination of forming limit curves. International Organization for Standardization; 2008. p. 20087.
- [24] Zhang L, Lin J, Sun L, Wang C, Wang L. A new method for determination of forming limit diagram based on digital image correlation. SAE technical paper 2013-01-1421. 2013.
- [25] Huang G, Sriram S, Yan B. Digital image correlation technique and its application in forming limit curve determination. In: Proc. of the IDDRG 2008 Int. Conference; 2008. p. 153–62.
- [26] Volk W, Hora P. New algorithm for a robust user-dependent evaluation of beginning instability for the experimental FLC determination. Int. J. Mater. Form. 2010;4:1–8.
- [27] Merklein M, Kuppert A, Geiger M. Time dependent determination of forming limit diagrams. CIRP annals 2010;59(1):295–8.
- [28] Hotz W, Merklein M, Kuppert A, Friebe H, Klein M. Time dependent FLC determination – comparison of different algorithms to detect the onset of unstable necking before fracture. Key Eng. Mater. 2013;549:397–404.
- [29] Li J, Carsley JE, Stoughton TB, Hector LGJr, Hu SJ. Forming limit analysis for two-stage forming of 5182-O aluminum sheet with intermediate annealing. Int. J. Plast. 2013;45:21–43.
- [30] Wang K, Carsley JE, He B, Li J, Zhang L. Measuring forming limit strains with digital image correlation analysis. J. Mater. Process. Technol. 2014;214:1120–30.
- [31] Fang S, Zheng X, Guo B, Sia B, Yang L. A new method for localized necking detection in uniaxial tensile testing based on a multi-camera DIC system. Mater. Today Commun. 2023;35:106021.
- [32] Zhang R, Shi Z, Shao Z, Dean TA, Lin J. A novel spatio-temporal method for determining necking and fracture strains of sheet metals. Int. J. Mech. Sci. 2021; 189:105977.
- [33] Szalai S, Harangozó D, Czinege I. Characterisation of Diffuse and Local Necking of Aluminium Alloy Sheets using DIC Technique. Acta Technica Jaurinensis 2019;12 (3):191–204.
- [34] El-Aty AA, Xu Y, Guo X, Zhang SH, Ma Y, Chen D. Strengthening mechanisms, deformation behavior, and anisotropic mechanical properties of Al-Li alloys: a review. J. Adv. Res. 2018;10:49–67.
- [35] Aleksandrovic S, Stefanovic M, Adamovic D, Lazic V. Variation of Normal Anisotropy Ratio "r" during Plastic Forming. Journal of Mechanical Engineering 2009;55(6):392–9.
- [36] You Z, Fu H, Qu S, Bao W, Lu L. Revisiting anisotropy in the tensile and fracture behavior of cold-rolled 316L stainless steel with heterogeneous nano-lamellar structures. Nano Materials Science 2020;2:72–9.
- [37] Eman J, Sundin KG, Oldenburg M. Spatially resolved observations of strain fields at necking and fracture of anisotropic hardened steel sheet material. Int. J. Solids. Struct. 2009;46:2750–6.
- [38] Tardif N, Kyriakides S. Determination of anisotropy and material hardening for aluminum sheet metal. Int. J. Solids. Struct. 2012;49:3496–506.

- [39] Chen K, Scales M, Kyriakides S, Corona E. Effects of anisotropy on material hardening and burst in the bulge test. Int. J. Solids. Struct. 2016;82:70–84.
- [40] Corallo L, Revil-Baudard B, Cazuca O, Verleysen P. Role of anisotropy on strain localization at high-strain rates in Ti6Al4V. European Journal of Mechanics /A Solids 2023;97:104856.
- [41] Marth S, Djebien S, Kajberg J, Haggblad HA. Stepwise modelling method for post necking characterisation of anisotropic sheet metal. Model. Simul. Mat. Sci. Eng. 2021;29:085001.
- [42] Rossi M, Broggiato GB, Papalini S. Application of digital image correlation to the study of planar anisotropy of sheet metals at large strains. Meccanica 2008;43: 185–99.
- [43] Ghosal P, Paul SK. Effect of specimen orientation to the rolling direction on uniaxial tensile forming and failure limits. Proc Inst Mech Eng, Part B: J Eng Manuf 2020;234(13):1598–603.
- [44] Abedini A, Butcher C, Worswick MJ. Fracture Characterization of Rolled Sheet Alloys in Shear Loading: studies of Specimen Geometry, Anisotropy, and Rate Sensitivity. Exp. Mech. 2017;57:75–88.
- [45] Seidi E, Miller S, Huang L, Stoughton T. Mathematical Analysis of the Tensile Behavior of DP 980 Steel Using Digital Image Correlation (DIC. In: Proceedings of the ASME 2023 18th International Manufacturing Science and Engineering Conference. 2: 2023. V002T06A038.
- [46] NCAL., NUMISHEET2020: benchmark Tests, 2020, Accessed June 16, 2022, Available from: https://www.tms.org/portal/MEETINGS_EVENTS/TMS_Meetin gs_Events/Upcoming_TMS_Meetings/NUMISHEET2021/benchmarkTests/porta l/Meetings_Events/2021/NUMISHEET2021/&10.18434/M32202.